



**HAL**  
open science

## Energetic Magnetospheric Particle Fluxes Onto Callisto's Atmosphere

Lucas Liuzzo, Andrew R Poppe, Peter Addison, Sven Simon, Quentin Nénon,  
Christopher Paranicas

► **To cite this version:**

Lucas Liuzzo, Andrew R Poppe, Peter Addison, Sven Simon, Quentin Nénon, et al.. Energetic Magnetospheric Particle Fluxes Onto Callisto's Atmosphere. *Journal of Geophysical Research Space Physics*, 2022, 127 (11), 10.1029/2022JA030915 . hal-04299677

**HAL Id: hal-04299677**

**<https://hal.science/hal-04299677>**

Submitted on 22 Nov 2023

**HAL** is a multi-disciplinary open access archive for the deposit and dissemination of scientific research documents, whether they are published or not. The documents may come from teaching and research institutions in France or abroad, or from public or private research centers.

L'archive ouverte pluridisciplinaire **HAL**, est destinée au dépôt et à la diffusion de documents scientifiques de niveau recherche, publiés ou non, émanant des établissements d'enseignement et de recherche français ou étrangers, des laboratoires publics ou privés.

# JGR Space Physics

## RESEARCH ARTICLE

10.1029/2022JA030915

### Key Points:

- We calculate the effect of Callisto's perturbed electromagnetic environment on energetic particle fluxes onto the top of the atmosphere
- Electron flux patterns are strongly affected by Callisto's plasma interaction, while ion fluxes are nearly uniform in the perturbed fields
- Fluxes onto the exobase are largest within the Jovian current sheet, despite strong field perturbations generated by the plasma interaction

### Correspondence to:







L. Liuzzo,  
liuzzo@berkeley.edu

### Citation:

Liuzzo, L., Poppe, A. R., Addison, P., Simon, S., N non, Q., & Paranicas, C. (2022). Energetic magnetospheric particle fluxes onto Callisto's atmosphere. *Journal of Geophysical Research: Space Physics*, 127, e2022JA030915. <https://doi.org/10.1029/2022JA030915>

Received 8 AUG 2022  
Accepted 10 NOV 2022

## Energetic Magnetospheric Particle Fluxes Onto Callisto's Atmosphere

Lucas Liuzzo<sup>1</sup> , Andrew R. Poppe<sup>1</sup> , Peter Addison<sup>2</sup> , Sven Simon<sup>2</sup> , Quentin N non<sup>3</sup> , and Christopher Paranicas<sup>4</sup> 

<sup>1</sup>Space Sciences Laboratory, University of California, Berkeley, CA, USA, <sup>2</sup>School of Earth and Atmospheric Sciences, Georgia Institute of Technology, Atlanta, GA, USA, <sup>3</sup>Institut de Recherche en Astrophysique et Plan tologie, CNRS-Universit  Toulouse III-CNES, Toulouse, France, <sup>4</sup>Applied Physics Laboratory, Johns Hopkins University, Laurel, MD, USA

**Abstract** This study investigates how Callisto's perturbed electromagnetic environment—generated by the moon's interaction with the low-energy Jovian magnetospheric plasma—affects the dynamics of high-energy ions and electrons. We constrain how these perturbed fields influence the energetic particle fluxes deposited onto the top of Callisto's atmosphere between energies of  $4.5 \text{ keV} \leq E \leq 11.8 \text{ MeV}$ . We use a hybrid simulation to model the variability in Callisto's perturbed electromagnetic environment over a synodic period by considering three representative scenarios of the moon's plasma interaction, corresponding to various distances of the moon to the Jovian magnetospheric current sheet. The local field perturbations are maximized near the center of the sheet (forming, e.g., signatures of field-line pileup, draping, and Alfv n wings) whereas far from the sheet, a mere superposition of the moon's induced dipole with the background field largely explains the perturbations. We then apply a test-particle approach to investigate the dynamics of energetic electrons and ions (protons, oxygen, and sulfur) while exposed to these fields. Since electron gyroradii are smaller than Callisto, the field perturbations generate small-scale non-uniformities in their flux patterns onto the moon, while the ion flux patterns are more homogeneous. Energetic electrons dominate the number flux onto the atmosphere, whereas ions dominate the energy flux. Over a synodic period, the flux patterns onto Callisto's exobase closely resemble those when the moon is near the current sheet center, since the differential energetic particle fluxes in the ambient plasma decrease by an order of magnitude when the moon travels far outside of the sheet.

**Plain Language Summary** Callisto's ambient plasma environment is comprised of low- and high-energy particles from Jupiter's magnetosphere that continually bombard the moon. Callisto's interaction with the low-energy population generates currents that locally perturb the electric and magnetic fields, the structures of which vary periodically over a full rotation of Jupiter. These perturbed electromagnetic fields, in turn, strongly affect the dynamics of the high-energy population—particles that are responsible for partially ionizing Callisto's atmosphere and sputtering the icy surface. This study constrains the degree to which these energetic ions and electrons are affected by Callisto's perturbed electromagnetic environment. We investigate how the high-energy irradiation of Callisto's atmosphere varies not only with latitude and longitude, but also throughout the moon's orbit around its parent planet. We show that the electron influx patterns strongly depend on Callisto's location within the Jovian magnetosphere, while the ion patterns are more robust against changes to the moon's local environment.

### 1. Introduction

Jupiter's second-largest moon, Callisto (radius  $R_C = 2,410 \text{ km}$ ), orbits the giant planet at an average distance of  $26.3R_J$  (radius of Jupiter  $R_J = 71,492 \text{ km}$ ). The Jovian magnetospheric plasma environment near Callisto can be characterized by two main populations: low-energy, thermal plasma with energies  $E$  below approximately  $E \leq 1 \text{ keV}$ , and higher-energy particles with kinetic energies that reach beyond  $E \gtrsim 10 \text{ MeV}$ . As Jupiter spins on its rotational axis, the magnetospheric field and the frozen-in, low-energy plasma continually bombard Callisto at a relative velocity of  $|\mathbf{u}_0| \approx 192 \text{ km/s}$  (Kivelson et al., 2004). Due to the  $\sim 9.6^\circ$  tilt between the giant planet's magnetic and rotational axes, properties of this thermal population vary over the course of a full synodic rotation. When Callisto is embedded within the Jovian current sheet, the local magnetospheric field mainly points southward with a magnitude of  $|\mathbf{B}_0| \approx 4 \text{ nT}$  (e.g., Kivelson et al., 1999), and the ambient plasma number density is on the order of  $n_0 \approx 0.1 \text{ cm}^{-3}$  (Bagenal & Delamere, 2011). However, the moon travels far outside of the sheet

throughout a synodic rotation, reaching distances on the order of  $\sim 4.5R_J$  above or below the center. At these locations, the magnetospheric field reaches strengths near the moon that are an order of magnitude larger than near the center ( $|\mathbf{B}_0| \approx 40$  nT; e.g., Khurana, 1997; Seufert et al., 2011), and mainly points either toward or away from the giant planet (Kivelson et al., 1999). The ambient plasma number density, on the other hand, drops by an order of magnitude compared to within the sheet, reaching values of  $n_0 \approx 0.01$  cm $^{-3}$  (Bagenal & Delamere, 2011; Kivelson et al., 2004).

As the properties of Callisto's local environment change over a synodic period, the interaction between the moon and the upstream plasma likewise varies. When located near the center of the Jovian current sheet, the interaction between the magnetospheric plasma and Callisto's atmosphere and ionosphere generates strong currents near the moon that cause the magnetospheric field to locally pile-up at the ramside (i.e., orbital trailing) hemisphere and drape around the obstacle. The associated perturbations in the electromagnetic fields can exceed the value of the background fields themselves (Liuzzo et al., 2015). Ionospheric particles newly generated by, for example, photoionization or electron impact ionization of Callisto's collisional atmosphere (Carberry Mogan et al., 2020; Cunningham et al., 2015; Hartkorn et al., 2017; Strobel et al., 2002) are picked-up by the ambient fields. As these ions gyrate and drift toward downstream, their feedback on the electromagnetic fields create additional perturbations to Callisto's local environment. Farther from the moon, the current system generated by this magnetosphere-ionosphere interaction is closed by currents that flow along the characteristics of Callisto's Alfvén wings (Neubauer, 1980, 1998), connecting the moon to Jupiter's polar ionosphere (e.g., Bhattacharyya et al., 2017).

As the Jovian current sheet sweeps over Callisto, the time variability of the ambient magnetospheric fields drives currents in conducting layers at the moon (i.e., a subsurface ocean and/or highly conductive, asymmetric ionosphere; e.g., Hartkorn & Saur, 2017; Vance et al., 2021; Zimmer et al., 2000). These induced currents manifest outside of the moon as a dipolar magnetic field (e.g., Styczinski et al., 2022). When located far outside the Jovian current sheet, the resulting interaction between the low-density magnetospheric plasma and Callisto's ionosphere and induced field is minor: field line pileup and draping only weakly affects the local electromagnetic field (Lindkvist et al., 2015; Liuzzo et al., 2015), and the induced dipole is the dominant source of magnetic field perturbations near Callisto (e.g., Khurana et al., 1998; Kivelson et al., 1999). At intermediate distances from the current sheet center, the non-linear coupling between the magnetosphere-ionosphere-dipole interaction generates perturbations with contributions from Callisto's induced dipole and mass loading from the moon's ionosphere: within the ramside region, signatures of pileup and draping are visible, while downstream of the moon, a quasi-dipolar “core region” is created where the induced field is nearly isolated from any plasma interaction effects and can explain the observed magnetic signatures (Liuzzo et al., 2016).

The interaction between Callisto and the low-energy thermal plasma generates electromagnetic field perturbations that map into the dynamics of the high-energy particles near the moon. Constraining the effects of these perturbed fields on the energetic population is therefore of utmost importance when investigating the irradiation of Callisto by these high-energy particles or when correlating observed features on the moon's icy surface to their precipitation patterns. To systematically represent the effect of the moon's plasma interaction on energetic particle dynamics in the perturbed fields, Liuzzo et al. (2019a, 2019b); modeled four scenarios for Callisto's perturbed environment: a superposition of an induced field at Callisto with the magnetospheric background field (i.e., without any plasma interaction currents), the magnetosphere-dipole interaction, the magnetosphere-ionosphere interaction, and a combined scenario with the magnetosphere-dipole-ionosphere interaction. These authors illustrated that the perturbed electromagnetic environment imprints clear signatures onto the dynamics of energetic ions and electrons and their precipitation patterns onto the moon's atmosphere. For example, the presence of the moon's induced dipole carves out minima in energetic ion patterns from regions with enhanced precipitation, and field-line pileup and draping partially shields Callisto's sub- and anti-Jovian apices from precipitation of energetic electrons. The goal of the studies by Liuzzo et al. (2019a, 2019b) was to isolate the effect that each aspect of Callisto's plasma interaction—the ionosphere and induced field—has on energetic particle dynamics. Hence, these studies used identical conditions for the magnetospheric plasma properties (i.e., the ambient number density, temperature, and magnetic field vector), while varying properties of Callisto as an obstacle with respect to the upstream flow (i.e., by including/removing the moon's induced field or ionosphere).

In addition, these previous studies investigated the *accessibility* of Callisto to energetic ions and electrons by presenting the precipitation patterns of these particles. Hence, while Liuzzo et al. (2019a, 2019b) studied how

changes to Callisto's plasma interaction affects the *patterns* of energetic ions and electrons as they precipitate onto the moon, they did not constrain the flux deposited onto the moon's atmosphere by this energetic particle population. This quantity is important in understanding processes including the energy deposition of these particles into the atmosphere or, after traveling through the collisional atmosphere, weathering and sputtering of the moon's icy surface (e.g., Vorburger et al., 2019). However, constraining the energetic particle flux onto the atmosphere requires taking into account properties of the ambient energetic particle distribution and requires an understanding of how this distribution is affected by the moon's locally perturbed environment. In addition, these studies did not consider the variability in the ambient plasma population itself and were thus unable to investigate the changes of energetic particle dynamics and precipitation patterns onto Callisto's atmosphere as a function of synodic period as the Jovian magnetospheric current sheet sweeps over the moon. Including these effects was beyond the scope of the studies by Liuzzo et al. (2019a, 2019b).

Therefore, the goal of this study is to quantify the energetic particle flux deposited onto the top of Callisto's atmosphere and to constrain the effect that changes to the perturbed electromagnetic environment over a synodic period have on these fluxes. To do so, we combine two established model frameworks that have been used to study Callisto's local environment: the AIKEF hybrid plasma model to constrain the moon's thermal plasma interaction, and the GENTOO test-particle model to investigate energetic particle dynamics and calculate the resulting fluxes. In Section 2, we describe the hybrid model and present key properties of Callisto's plasma interaction over a synodic period, while in Section 3 we present the test-particle approach that is used to investigate energetic particle dynamics and fluxes, and provide a brief primer on the ambient energetic particle environment near the moon. Section 4 presents results from the particle tracing model, including the fluxes of energetic particles onto the top of Callisto's atmosphere and the variability associated with the changing plasma interaction over a synodic period. An analysis regarding the implications of our findings, along with a discussion on the structure of the flux patterns onto Callisto's exobase averaged over a full synodic period, is presented in Section 5, while Section 6 concludes the study.

## 2. Modeling Callisto's Perturbed Electromagnetic Environment

To constrain the structure of Callisto's perturbed electromagnetic environment, we apply the *Adaptive Ion-Kinetic, Electron-Fluid* model (AIKEF; Liuzzo et al., 2015; Müller et al., 2011). AIKEF applies a hybrid technique, in which ions are treated as individual particles while electrons are treated as a massless, charge-neutralizing fluid. The hybrid approach allows for the resolution of ion-kinetic effects including, for example, non-Maxwellian distributions, flow shear between multiple plasma species, and the effects of large ion gyroradii. Such a kinetic treatment of ions is necessary to obtain an accurate picture of Callisto's electromagnetic environment: the gyroradii of ionospheric particles drastically exceed the radius of the moon itself (e.g., the gyroradius  $r_g$  of an  $\text{O}_2^+$  ion can exceed  $r_g \approx 10R_C$ ; see Liuzzo et al., 2015). The effects of the non-negligible ion gyration generates notable asymmetries in the electromagnetic fields near the moon (e.g., Liuzzo et al., 2016, 2017, 2018).

Within the model, we include the  $\text{CO}_2$  and  $\text{O}_2$  components of Callisto's atmosphere, describing each using a barometric law with scale heights on the order of  $0.1R_C$  (see Liuzzo et al., 2015). The resulting atmospheric structure is consistent with Hubble Space Telescope and Galileo spacecraft observations of these components (e.g., Carlson, 1999; Cunningham et al., 2015). Although additional, minor components of the moon's atmosphere may be present (e.g., hydrogen; see Carberry Mogan et al., 2020, 2021; Roth et al., 2017), they likely do not strongly contribute to the global features associated with Callisto's plasma interaction since they are much lighter than the  $\text{CO}_2$  and  $\text{O}_2$  components and have surface densities that are likely orders of magnitude below these dominant species. Within AIKEF, this atmosphere is ionized via photoionization (by applying the solar EUV flux model for aeronomic calculations; see Richards et al., 1994), along with a minor contribution from impact ionization by low-energy electrons and charge exchange with the incident magnetospheric plasma (for further details on the treatment of the atmosphere and ionosphere within AIKEF, see Liuzzo et al., 2015).

In addition to the moon's atmosphere and ionosphere, we also include Callisto's induced field within the AIKEF simulations. We note that while the specific region within which significant induction occurs is under debate (i.e., within a subsurface ocean, an ionosphere with scale height  $\ll R_C$ , or some combination thereof; cf., Hartkorn & Saur, 2017; Khurana et al., 1998; Vance et al., 2021), the presence of an inductive response visible above the moon's ionosphere is certain: a dipolar signature has been observed during multiple flybys of Callisto by the Galileo spacecraft (e.g., Kivelson et al., 1999; Liuzzo et al., 2015, 2016). These observations are consistent with

**Table 1**  
*Parameters of the Hybrid Simulations Used in This Study*

|                                                      | Max. above sheet (north)                        | Within sheet                                 | Max. below sheet (south)                        |
|------------------------------------------------------|-------------------------------------------------|----------------------------------------------|-------------------------------------------------|
| $\mathbf{B}_0$ (nT)                                  | $[-2.0\hat{x} - 29.3\hat{y} - 6.6\hat{z}]$      | $[+0.0\hat{x} + 0.0\hat{y} - 4.0\hat{z}]$    | $[+9.0\hat{x} + 35.3\hat{y} - 6.6\hat{z}]$      |
| $ \mathbf{B}_0 $ (nT)                                | 30.1                                            | 4.0                                          | 37.0                                            |
| $\mathbf{M}_0$ ( $\cdot 10^{18}$ Am <sup>2</sup> )   | $[+0.14\hat{x} + 2.05\hat{y} + 0.0\hat{z}]$     | $[+0.0\hat{x} + 0.0\hat{y} + 0.0\hat{z}]$    | $[-0.63\hat{x} - 2.50\hat{y} + 0.0\hat{z}]$     |
| $ \mathbf{M}_0 $ ( $\cdot 10^{18}$ Am <sup>2</sup> ) | 2.05                                            | 0                                            | 2.58                                            |
| $\mathbf{v}_{A,0}$ (km/s)                            | $[-54.53\hat{x} - 798.9\hat{y} - 179.9\hat{z}]$ | $[+0.0\hat{x} + 0.0\hat{y} - 55.64\hat{z}]$  | $[+245.4\hat{x} + 962.5\hat{y} - 179.9\hat{z}]$ |
| $ \mathbf{v}_{A,0} $ (km/s)                          | 820.7                                           | 55.64                                        | 1,009                                           |
| $\mathcal{Z}^+$ (km/s)                               | $[+137.4\hat{x} - 798.9\hat{y} - 179.9\hat{z}]$ | $[+192.0\hat{x} + 0.0\hat{y} - 55.6\hat{z}]$ | $[+437.4\hat{x} + 962.5\hat{y} - 179.9\hat{z}]$ |
| $\mathcal{Z}^-$ (km/s)                               | $[+246.5\hat{x} + 798.9\hat{y} + 179.9\hat{z}]$ | $[+192.0\hat{x} + 0.0\hat{y} + 55.6\hat{z}]$ | $[-53.40\hat{x} - 962.5\hat{y} + 179.9\hat{z}]$ |
| $n_0$ (cm <sup>-3</sup> )                            | 0.04                                            | 0.1537                                       | 0.04                                            |
| $\beta_i$                                            | 0.01                                            | 16.0                                         | 0.01                                            |
| $M_A$                                                | 0.23                                            | 3.45                                         | 0.19                                            |
| $M_{MS}$                                             | 0.23                                            | 0.83                                         | 0.19                                            |
| $M_S$                                                | 2.10                                            | 0.86                                         | 2.10                                            |

*Note.* Included are values for the magnetospheric background field  $\mathbf{B}_0$ , Callisto's induced magnetic moment  $\mathbf{M}_0$ , the local Alfvén velocity  $\mathbf{v}_{A,0}$ , Alfvén wing characteristics  $\mathcal{Z}^\pm = \mathbf{u}_0 \pm \mathbf{v}_{A,0}$ , magnetospheric plasma number density  $n_0$  and ion plasma beta  $\beta_i$ , and the Alfvénic, magnetosonic, and sonic Mach numbers,  $M_A$ ,  $M_{MS}$ , and  $M_S$ , respectively. Values for  $\mathbf{B}_0$  are obtained from the Jovian VIP4 (Connerney et al., 1998) internal field model plus the Khurana (1997) current sheet field and values for  $n_0$  are obtained from Bagenal and Delamere (2011). The values for  $\mathbf{M}_0$  are calculated assuming a perfect conductor of radius  $1R_C$ , (see also Khurana et al., 1998; Liuzzo et al., 2016; Zimmer et al., 2000).

the inductive response of a perfect conductor with radius  $r = R_C$  that, while constant on the  $\sim$ hour-long timescale of an individual encounter, varies on a flyby-to-flyby basis. Therefore, although the source region of this inductive signal may be uncertain, we represent Callisto's induced magnetic field within the model using a magnetic moment  $\mathbf{M}_0$  that is centered at the moon with an amplitude  $A = 1$  and a phase lag of  $\phi = 0$  (see also Zimmer et al., 2000). On the minutes-long timescale over which the plasma interaction occurs, the induced field can be treated as temporally constant.

For this study, we represent the change in the ambient magnetospheric environment near Callisto over a synodic period using three discrete positions of the moon with respect to the center of the Jovian current sheet. These correspond to times when the moon is located at its maximum distance above the sheet (approximately  $4.5R_J$  north of the center, near a System III longitude of  $\lambda_{III} \approx 210^\circ$ ), embedded within the center of the sheet (where  $\lambda_{III} \approx 120^\circ$  or  $\lambda_{III} \approx 300^\circ$ ), and at its maximum distance below the sheet (approximately  $-4.5R_J$  south of the center, with  $\lambda_{III} \approx 30^\circ$ ). To obtain the ambient magnetospheric field vector near Callisto at each of the three locations, we apply a combination of the VIP4 model for Jupiter's internal field (Connerney et al., 1998) plus the Khurana (1997) model of the magnetospheric current sheet. Since Callisto's interaction with the magnetospheric plasma does not display a strong dependence with respect to local time in the moon's orbit around Jupiter (see Liuzzo et al., 2015), we assume that Callisto is located at dusk (i.e., at 18:00 local time) for all cases presented herein. To obtain the magnetospheric plasma number density as a function of distance to the center of the current sheet, we apply the model of Bagenal and Delamere (2011). The resulting parameters of the magnetospheric plasma assumed for each of the three hybrid simulations are included in Table 1. Vector quantities are presented using the Callisto-centered CphiO system: unit vector  $\hat{x}$  is aligned with the direction of corotation (and the direction of Callisto's orbital motion), unit vector  $\hat{y}$  points toward Jupiter, and unit vector  $\hat{z}$  completes the right-handed, Cartesian system. All simulations use a box size of  $30R_C$  with Callisto located at the center, with a grid resolution of  $0.05R_C$  at the finest level of refinement. For each case, we set the ion mass to  $m_0 = 16$  amu and use a bulk velocity of  $\mathbf{u}_0 = 192\hat{x}$  km/s (i.e., approximately 60% of the local corotation velocity as is expected from the breakdown of corotation at Callisto's orbital distance and is consistent with the bulk velocities observed by the Galileo and Voyager missions at these distances; e.g., Belcher, 1983; Kivelson et al., 2004).

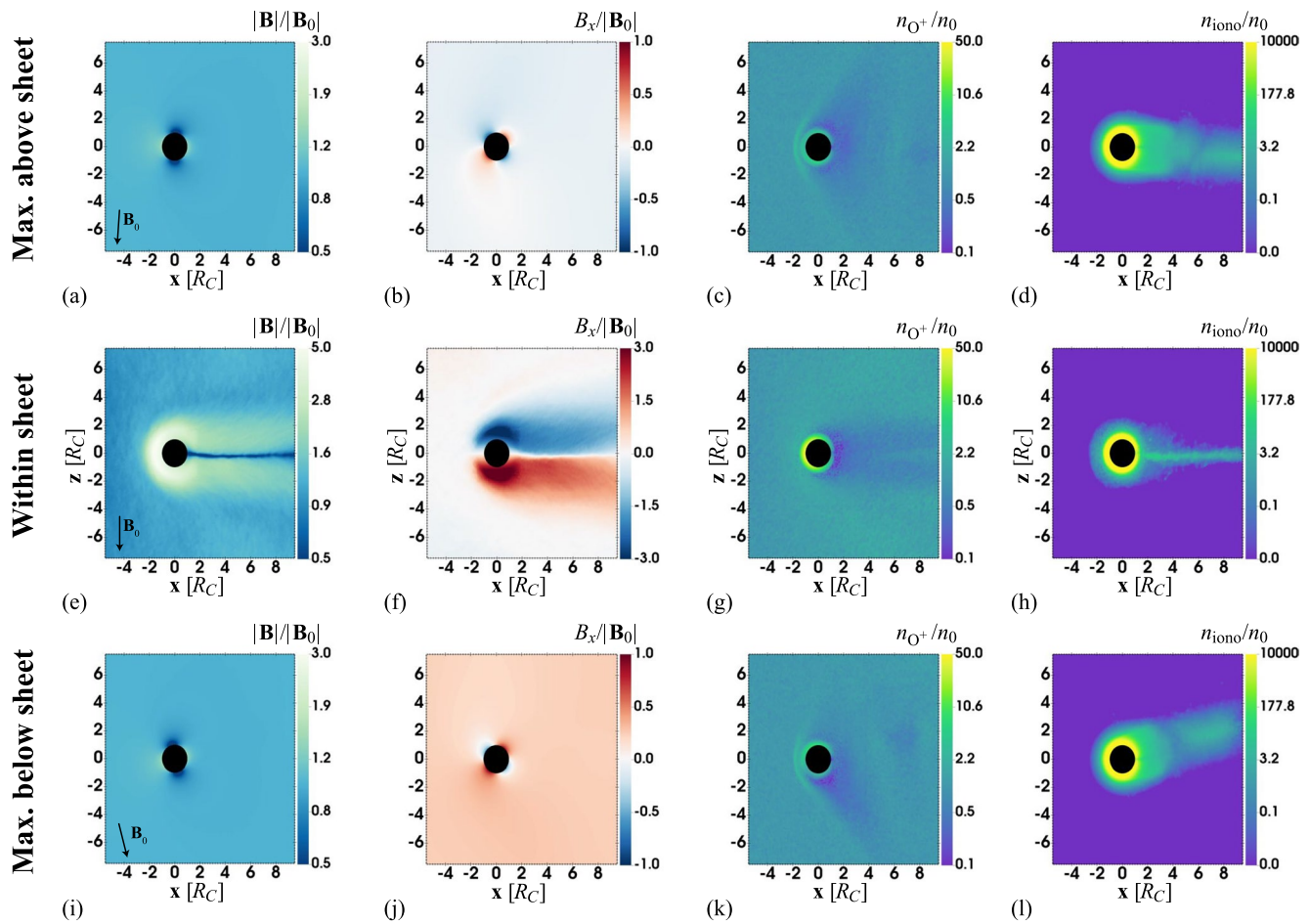


**Figure 1.** Callisto's perturbed electromagnetic environment in planes containing the ambient flow vector  $\mathbf{u}_0$ , magnetospheric background field  $\mathbf{B}_0$ , and the center of the moon. Rows correspond to the three scenarios considered in this study (top row; a–d) at the maximum distance above the center of the Jovian current sheet, (center row; e–h) embedded within the sheet, and (bottom row; i–l) at the maximum distance below the center of the sheet. Displayed from left to right are the magnetic field magnitude, flow-aligned component of the magnetic field, upstream ( $O^+$ ) ion number density, and ionospheric ( $CO_2^+$  plus  $O_2^+$ ) ion number density, respectively, normalized to the background magnetic field or density value (see Table 1). Note that for the case of Callisto within the sheet (middle row), the cutting plane shown here coincides with the  $(x, z)$  plane of the CphiO system; for the cases above and below the sheet, the vertical axis does not correspond to any axis of CphiO. Note the different ranges to the color scales used for the magnetic field quantities above and below the sheet (top and bottom rows) compared to within it (center row).

Figures 1 and 2 illustrate the variability in Callisto's interaction with its ambient plasma environment when located (a–d; top row) at maximum distance above the center of the magnetospheric current sheet (e–h; middle row) within the sheet, and (i–l; bottom row) at maximum distance below the sheet. For each figure, the left two columns display the magnitude and flow-aligned (i.e.,  $x$ ) component of the magnetic field, respectively, while the right two columns show the number density of the upstream ( $+$ ) and total ionospheric ( $CO_2^+$  plus  $O_2^+$ ) plasma species, respectively. To facilitate a straightforward comparison between the three simulations, all quantities are normalized to the magnetic field or density value of the background plasma ( $|\mathbf{B}_0|$  or  $n_0$ , provided in Table 1). Figure 1 displays a cross section through the center of Callisto in a plane that contains the ambient flow velocity vector ( $\mathbf{u}_0$ ; along  $+\hat{x}$  for each simulation) and the magnetic field direction ( $\mathbf{B}_0$ ; with direction provided in the lower left of panels a, e, and i). Figure 2 displays identical quantities as Figure 1, but in the plane containing the flow velocity and the convective electric field direction ( $\mathbf{E}_0 = -\mathbf{u}_0 \times \mathbf{B}_0$ ). Note that within the center of the current sheet, the magnetospheric background field points along the  $-\hat{z}$  direction, so the vertical axes in panels 1e–1h and 2e–2h correspond to the  $\hat{z}$  and  $\hat{y}$  axes of the CphiO system, respectively.

When Callisto is located at maximum distances above or below the center of the Jovian current sheet, Figures 1 and 2 illustrate that the moon's magnetic environment is only weakly perturbed by the interaction between the magnetospheric plasma and Callisto's ionosphere and induced dipole. The most obvious perturbation above the

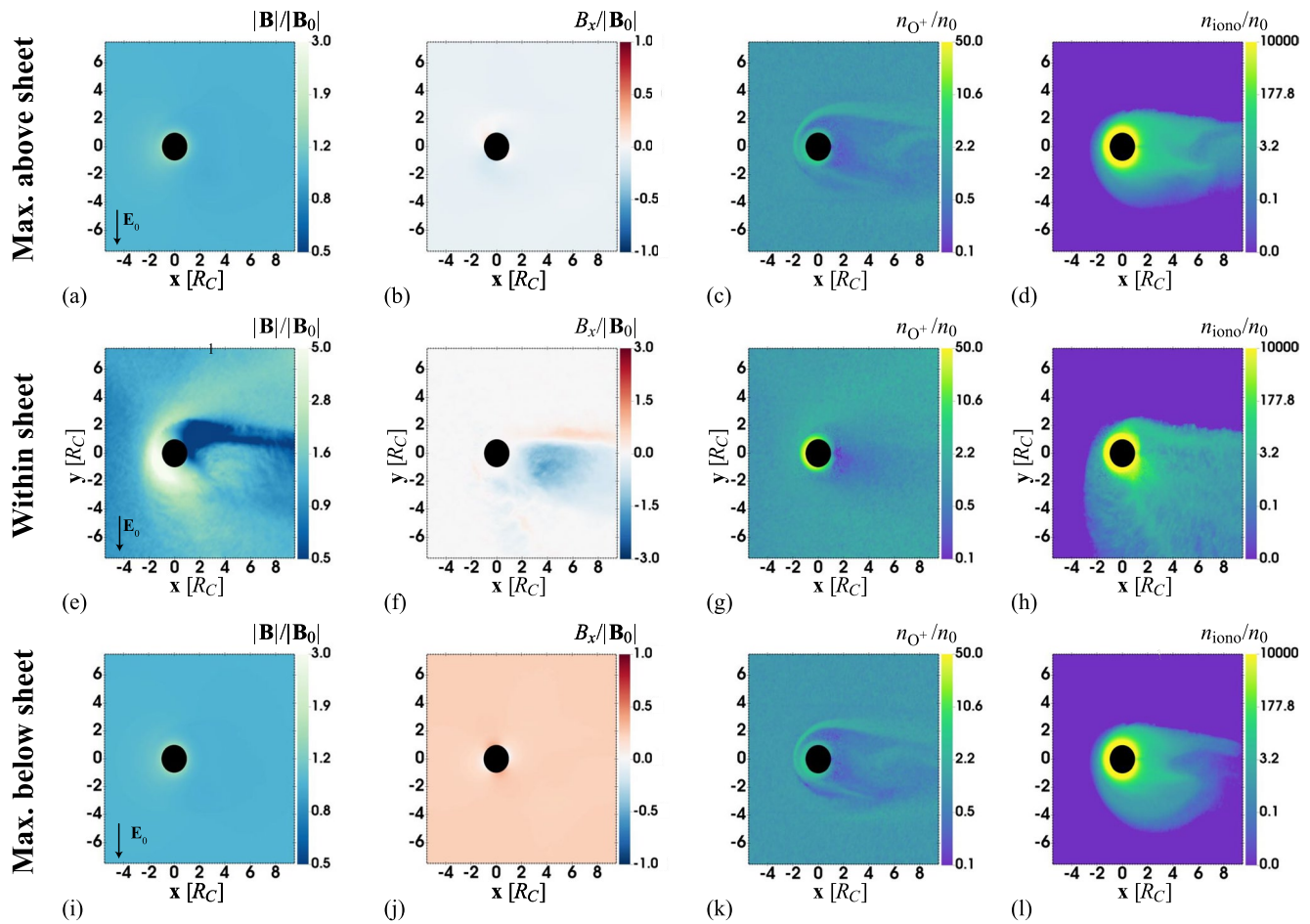


**Figure 2.** Callisto's perturbed electromagnetic environment in planes containing the ambient flow vector  $\mathbf{u}_0$ , convective electric field  $\mathbf{E}_0 = -\mathbf{u}_0 \times \mathbf{B}_0$ , and the center of the moon. For the case of Callisto within the current sheet, the vertical axis corresponds with  $\hat{y}$  of the CphiO system. See Figure 1 for further details.

background value in panels 1a, 1i, 2a, and 2i is caused by the induced field. Since the induced magnetic moment is anti-parallel to the magnetospheric background field, the superposition generates a region of reduced field strength  $|\mathbf{B}|$  near the “poles” of the moon's induced dipole (dark blue hues), while the field strength is enhanced near Callisto's “magnetic equator” (yellow hues). Similarly, the  $B_x$  component shows the “shamrock leaf”-like signatures of Callisto's induced field when the moon is located far outside of the current sheet, where the magnetic field displays alternating regions of (reds)  $B_x > 0$  and (blues)  $B_x < 0$ . These features arise from the superposition between an induced dipole field and a background field, with similar signatures identified at Callisto by, for example, Liuzzo et al. (2019a, 2019b).

Within the center of the Jovian current sheet, however, the magnetic field near Callisto is strongly perturbed compared to the other two cases (see the middle rows of Figures 1 and 2). Upstream of Callisto at the moon's orbital trailing apex, the local field strength exceeds the value of the background field by a factor of  $\sim 5$ , and the pileup region displays a strong asymmetry along the direction of the convective electric field (see Figure 2e). Figure 1e highlights that in the plane containing  $\mathbf{B}_0$ , the magnetic field strength is reduced to values below  $0.5|\mathbf{B}_0|$  within a thin magnetic “neutral sheet” downstream of the moon. In the plane perpendicular to  $\mathbf{B}_0$ , Figure 2e illustrates that this wakeside neutral region is noticeably asymmetric, extending nearly  $2R_C$  into the moon's sub-Jovian (+y) hemisphere. As with  $|\mathbf{B}|$ , the  $B_x$  component is perturbed by the magnetospheric interaction with Callisto's ionosphere (see panels 1f and 2f), with strong signatures of field-line draping and Alfvén wings extending further from the moon along characteristics tilted at an angle of  $\tan^{-1}M_A \approx 74^\circ$  against the background field.

In the plane containing  $\mathbf{B}_0$ , panels 1c, 1g, and 1k illustrate that the number density of the magnetospheric plasma is maximized at Callisto's ramside (i.e., orbital trailing) hemisphere. As it approaches Callisto, the magnetospheric

plasma is mass loaded and the continuity equation dictates that the resulting plasma slowdown coincides with an enhanced magnetospheric plasma density. Since this plasma is deflected around the moon and out of the  $\mathbf{u}_0\text{-}\mathbf{B}_0$  plane displayed in Figure 1, a wakeside cavity forms downstream where  $n_{O^+}$  is reduced below its background value. In addition, the number density of the ionospheric species exceeds the upstream plasma density by more than two orders of magnitude near the moon for all three distances to the center of the Jovian current sheet. In the plane containing the magnetic field (Figure 1), outflow of the ionospheric particles is nearly symmetric, and is rotated against  $\mathbf{u}_0$  such that the direction of outflow remains nearly perpendicular to  $\mathbf{B}_0$  for all three cases. For the case with Callisto located near the center of the current sheet, the ionospheric pickup tail is narrow and confined to the magnetic neutral sheet downstream of the moon where the magnetic pressure is reduced (see panel 1h). However, the plane perpendicular to the magnetic field (Figure 2) further highlights the importance of capturing effects of large ion gyroradii near Callisto: in the plane perpendicular to the magnetic field, gyration and outflow of the heavy ionospheric particles generates an asymmetric cycloidal outer shape of the pickup tail in the  $y < 0$  half space (i.e., along the  $\mathbf{E}_0$  direction). In the case of Callisto located near the center of the magnetospheric current sheet, these asymmetries are also clearly imprinted on the magnetic field perturbations (see discussion of panel 2e above). Concurrently, momentum conservation causes the magnetospheric ions to be accelerated into the  $-\mathbf{E}_0$  direction corresponding to an enhancement in  $n_{O^+}$  by a factor of nearly 10 in the sub-Jovian hemisphere, as is especially visible in the cases with Callisto at maximum distances from the Jovian current sheet (see panels 2c and 2k).

Notably, panel 1k shows that with Callisto located at maximum distance below the current sheet, the region where the magnetospheric plasma density is most depleted in the  $\mathbf{u}_0\text{-}\mathbf{B}_0$  plane does not coincide within the moon's geometric plasma shadow. Instead, the density depletion is rotated out of the expected wake location toward the  $\mathcal{Z}^+$  ( $= \mathbf{u}_0 + \mathbf{v}_{A,0}$ ) Alfvén wing characteristic. For this case, the Alfvénic Mach number of the magnetospheric plasma is  $M_A = 0.19$ , and the background field is tilted at an angle of  $76^\circ$  against the magnetospheric flow direction (i.e., rotated  $14^\circ$  away from the  $\mathbf{u}_0 \perp \mathbf{B}_0$  case, toward the moon's downstream hemisphere; see, e.g., Equation 4 of Neubauer, 1980 or Equations 1 and 2 of Simon et al., 2022). This minor deviation rotates the  $\mathcal{Z}^-$  ( $= \mathbf{u}_0 - \mathbf{v}_{A,0}$ ) Alfvén wing characteristic into Callisto's upstream hemisphere (see also Table 1). In turn, deflection of the upstream magnetospheric plasma around this characteristic is directed *toward* Callisto, the absorption of which forms a plasma wake that is displaced out of the moon's downstream hemisphere. To date, such a feature has only been theoretically predicted to occur at Neptune's moon, Triton (see Liuzzo et al., 2021). Simon et al. (2022) have shown analytically that such a feature can form if this deviation exceeds a “critical angle,” given by  $\theta_c = \arcsin(M_A)$ . For these conditions with Callisto at maximum distances below the magnetospheric current sheet,  $\theta_c = 11^\circ$ , and yet, in this case of Callisto's interaction far below the magnetospheric current sheet, the deviation of the magnetospheric field against the scenario of  $\mathbf{u}_0 \perp \mathbf{B}_0$  reaches an angle of  $14^\circ$ . Hence, this deviation is a further  $3^\circ$  beyond the critical angle required for an Alfvén-wing-generated displaced wake to form at Callisto. Note that a similar feature is *not* visible in panel 1c with Callisto located far above the magnetospheric current sheet. As illustrated in Table 1, the  $B_{x,0}$  and  $B_{y,0}$  components of the magnetic field are not mirrored between the maximum distance above or below the center of the current sheet, likely caused by the asymmetric effect of the hinging of the magnetospheric current sheet near Callisto's orbital position (see, e.g., Khurana, 1992, 1997). Hence, for the case of Callisto located far above the current sheet, the angle between the magnetospheric background field and flow velocity vectors is  $86^\circ$ ; that is, it is only rotated by an angle of  $4^\circ$  toward upstream. However, since the critical angle  $\theta_c = \arcsin(0.23) = 13^\circ$  is not reached for this case, both characteristics point toward downstream (see Table 1) and an Alfvén-wing-driven absorption feature does not form under these conditions.

### 3. Modeling Energetic Particles Near Callisto

The ultimate goal of this research is to investigate the energetic particle fluxes onto Callisto in order to understand their energy deposition into the moon's atmosphere and constrain the weathering and radiolysis of the moon's icy surface over the course of a synodic period. The approach used herein to study energetic particle dynamics (discussed in Sections 3.1 and 3.2 below) applies Liouville's theorem. This method allows us to convert energetic particle distributions measured in the unperturbed flow outside of Callisto's interaction region into fluxes deposited onto a certain location near the moon, while concurrently considering the effect that the perturbed electromagnetic environment—generated by the moon's interaction with the low-energy, thermal plasma—has on energetic particle dynamics. However, once an energetic charged particle passes below Callisto's exobase



where it may potentially collide with a neutral particle, Liouville's theorem is no longer applicable to determine the flux it carries. Therefore, in order to accurately represent the energetic particle flux onto Callisto's surface, the energy deposited by these particles into the collisional atmosphere must first be constrained. Such an effort requires tracing the particles through the moon's atmosphere while including a mechanism to represent the energy loss of each particle as it interacts with the neutral gas envelope using, for example, a statistical (e.g., Addison et al., 2021; Kotova et al., 2015) or continuous (e.g., Kabanovic et al., 2018; Modolo & Chanteur, 2008; Snowden & Yelle, 2014; Wulms et al., 2010) approach.

As a first step, this study will therefore identify the trajectories of energetic particles that are able to access the top of Callisto's atmosphere and quantify the flux associated with their precipitation, thereby constraining how the moon's perturbed electromagnetic environment (see Section 2) affects energetic particle accessibility and fluxes onto the exobase. In a later investigation, we plan to use the positions, velocities, and fluxes of such particles at the top of the atmosphere—as identified by this study—as initial conditions for a separate model that will calculate the energy deposition associated with particles passing through Callisto's neutral gas envelope. Such an approach would capture, for instance, the dynamics of particles that only briefly “dive” beneath the exobase but subsequently exit the atmosphere again. Finally, using these results, the energy deposition into, and sputtering of, Callisto's icy surface can be studied. While understanding the interaction of energetic magnetospheric particles with Callisto's atmosphere and surface is therefore beyond the scope of this study, it will be presented in future investigations.

We again emphasize that the properties of the magnetospheric plasma used for the three distances of Callisto with respect to the current sheet as input into the AIKEF model (see Table 1) represent the range of plasma conditions near the moon during a full synodic period of Jupiter (see also the variability listed in, e.g., Bagenal et al., 2016; Kivelson et al., 2004). However, using exact properties of the local plasma environment at a given snapshot in time is not necessary for this study. Instead, the particle fluxes calculated in this way are suitable to describe processes that take place on long timescales, such as surface erosion by the portion of the energetic particle influx that can penetrate through the atmosphere. The following results should therefore be interpreted as representing the energetic particle fluxes onto Callisto's exobase over such timescales, which are relevant for such effects.

Finally, we note that within the hybrid simulations, we model Callisto's inductive response as a global dipolar signature (see also Liuzzo et al., 2015, 2016; Zimmer et al., 2000). While such a response does not accurately represent the local field induced within Callisto's ionosphere, we only trace energetic ion and electron dynamics while they are located *outside* of the ionosphere. Since the atmospheric and ionospheric scale heights (on the order of 10–100s of km; see, e.g., Carberry Mogan et al., 2021; Kliore et al., 2002) are small compared to the size of Callisto, assuming a global, dipolar inductive response is reasonable at altitudes beyond the exobase (i.e., at altitudes above the inner boundary of the energetic particle simulations; see Section 3.1 below). Indeed, Hartkorn and Saur (2017) have shown that for two of the Galileo flybys where a strong inductive signature was observed at altitudes above the ionosphere, a global dipolar response from a subsurface ocean explains magnetometer data equally as well as a field induced within the ionosphere. Hence, any fine-structures to Callisto's inductive response that are generated within the ionosphere are “smeared-out” at higher altitude and the resulting signature is nearly dipolar. Such localized, fine-scale signatures therefore have only a minimal effect on the global energetic particle precipitation patterns and fluxes onto the top of the atmosphere.

### 3.1. Tracing Energetic Particle Dynamics: The GENTOO Model

To solve for the dynamics of energetic ions and electrons as they precipitate onto Callisto's atmosphere, we use the *Galilean Energetics Tracing Model* (GENTOO; Liuzzo et al., 2019a, 2019b). GENTOO has been used to study energetic particle dynamics near each of the icy Galilean moons (Addison et al., 2021, 2022; Breer et al., 2019; Liuzzo et al., 2019a, 2019b), so only a brief discussion of the model is provided here. GENTOO imports the locally perturbed electromagnetic fields near Callisto as calculated by the AIKEF hybrid model and solves the relativistic Lorentz force equation to calculate the dynamics of energetic test particles using the approach introduced by Vay (2008), which applies a second-order leapfrog solver to advance the particles within the simulation. This method corrects for the large errors present in the method introduced by Boris (1970) when solving for the trajectories of relativistic particles. For each simulation, the time step used is a small fraction of the particle's gyroperiod and the Vay (2008) method is able to reproduce the gyration and drift motion of charged particles in uniform fields with an error well below 0.01% compared to the analytical solution. Hence, the largest source

**Table 2**  
Range of Relativistic Lorentz Factors  $\gamma$  and Gyroradii  $r_g$  for Electrons and Ions at the Ten Energies Considered in This Study

| E (keV) | e <sup>-</sup> |            | H <sup>+</sup> |            | O <sup>2+</sup> |            | S <sup>3+</sup> |            |
|---------|----------------|------------|----------------|------------|-----------------|------------|-----------------|------------|
|         | $\gamma$       | $r_g(R_C)$ | $\gamma$       | $r_g(R_C)$ | $\gamma$        | $r_g(R_C)$ | $\gamma$        | $r_g(R_C)$ |
| 4.5     | 1.01           | 0.003–0.02 | 1.00           | 0.11–1.01  | 1.00            | 0.22–2.01  | 1.00            | 0.20–1.90  |
| 12      | 1.02           | 0.004–0.04 | 1.00           | 0.18–1.64  | 1.00            | 0.35–3.28  | 1.00            | 0.33–3.10  |
| 32      | 1.06           | 0.007–0.06 | 1.00           | 0.29–2.70  | 1.00            | 0.58–5.36  | 1.00            | 0.55–5.06  |
| 80      | 1.16           | 0.011–0.10 | 1.00           | 0.46–4.24  | 1.00            | 0.92–8.48  | 1.00            | 0.86–7.99  |
| 221     | 1.43           | 0.02–0.18  | 1.00           | 0.76–7.05  | 1.00            | 1.52–14.1  | 1.00            | 1.44–13.3  |
| 577     | 2.13           | 0.04–0.33  | 1.00           | 1.23–11.4  | 1.00            | 2.46–22.8  | 1.00            | 2.32–21.5  |
| 1,517   | 3.97           | 0.07–0.68  | 1.00           | 2.00–18.5  | 1.00            | 3.99–36.9  | 1.00            | 3.76–34.8  |
| 3,551   | 7.95           | 0.15–1.39  | 1.00           | 3.05–28.3  | 1.00            | 6.10–56.5  | 1.00            | 5.76–53.3  |
| 6,878   | 14.5           | 0.28–2.55  | 1.01           | 4.26–39.4  | 1.00            | 8.60–78.6  | 1.00            | 8.01–74.1  |
| 11,798  | 24.1           | 0.46–4.26  | 1.01           | 5.58–51.7  | 1.00            | 11.1–103   | 1.00            | 10.5–97.1  |

*Note.* Maximum and minimum values for each particle's gyroradius correspond to the minimum and maximum magnetic field magnitude near Callisto's orbit, dependent on the moon's distance to the center of the Jovian magnetospheric current sheet (using either  $|\mathbf{B}_0| = 4$  nT or  $|\mathbf{B}_0| = 37$  nT; see Table 1). All gyroradii values are calculated using a pitch angle of  $\alpha = 90^\circ$ .

of error in our results is not numerical, but is rather associated with any uncertainties of the range of the plasma properties near Callisto. To optimize computational efficiency, GENTOO initializes particles on a concentric sphere around Callisto and traces their dynamics *backwards* in time (time step  $dt < 0$ ), thereby avoiding the tracing of particles that may never encounter the moon's perturbed electromagnetic environment.

In this study, we focus on energetic particles at energies between  $4.5 \text{ keV} \leq E \leq 11.8 \text{ MeV}$ , consistent with previous studies that have investigated energetic particle dynamics near the icy Galilean moons (e.g., Fatemi et al., 2016; Liuzzo et al., 2019a, 2019b; Plainaki et al., 2015, 2020; Vorburger et al., 2022). The differential fluxes of ions and electrons with energies beyond  $E \geq 11 \text{ MeV}$  are more than five orders of magnitude lower than the fluxes near  $E = 4.5 \text{ keV}$  (see Section 3.2 below). Hence, the contribution of particles at even higher energies to the total flux onto Callisto's atmosphere is negligible in comparison to the contribution from particles at these lower energies. We discretize the energy range into 10 values as provided in Table 2, such that the change in energy is approximately logarithmic (see also Liuzzo et al., 2020). Note that the Lorentz factor  $\gamma$  remains below  $\gamma < 1.01$  for the magnetospheric ions throughout the entire energy range considered. We investigate the dynamics of energetic electrons as well as H<sup>+</sup>, O<sup>2+</sup>, and S<sup>3+</sup> ions. Although the average dominant charge state of energetic oxygen ions (O<sup>1+</sup> vs. O<sup>2+</sup>) and sulfur ions (S<sup>2+</sup> vs. S<sup>3+</sup>) near Callisto is under debate (cf., e.g., results presented in Bagenal et al., 2016; Clark et al., 2016, 2020; Collier & Hamilton, 1995; Cooper et al., 2001; Keppler & Krupp, 1996), changing their charge state by one would likely only generate a minor change to the ion flux patterns (see Addison et al., 2021; Liuzzo et al., 2019b). In addition, the use of O<sup>2+</sup> and S<sup>3+</sup> in our model facilitates a straightforward comparison with previous studies of energetic particle dynamics near the icy Galilean moons (e.g., Addison et al., 2021, 2022; Liuzzo et al., 2019a, 2019b, 2020; Plainaki et al., 2015; Poppe et al., 2018).

For each of the four species, and at each of the 10 energies considered, particles are initialized on a spherical starting grid at a spatial resolution of  $2^\circ$  in latitude and  $4^\circ$  in longitude. This grid is located at an altitude of  $0.1R_C = 241 \text{ km}$  above Callisto's surface, which corresponds to the approximate location of the moon's exobase (see, e.g., Carberry Mogan et al., 2021). At each point on this grid, particles are injected at a given velocity (with magnitude determined by their starting energy) at an angular resolution of  $2^\circ$  in azimuth and  $4^\circ$  in elevation. Hence, 8,100 particles are initialized at each point of the starting grid, yielding more than 65 million particles for every simulation.

Two outcomes are possible for each particle that is traced backward in time during a given GENTOO simulation. If, at any time, a backtraced particle is located *below* the starting grid (i.e., with its position  $|\mathbf{r}| < 1.1R_C$ ), its trajectory is *forbidden* and it is removed from the simulation (since this particle does not possess a valid trajectory in a forward tracing approach). Since this starting grid is coincident with Callisto's exobase, a particle that travels

below this point is likely to undergo a collision and lose energy, a physical process that is not captured in the approach used by the GENTOO model. Alternatively, if a particle's position never again intersects the starting grid after initialization, its trajectory is *allowed* and the particle contributes to the flux onto Callisto's atmosphere. Yet, final characterization of a trajectory as allowed requires special consideration. The electromagnetic field perturbations near Callisto vanish at a distance of approximately  $10R_c$  from the moon (see Figures 1 and 2), and the hybrid simulation domain extends to  $\pm 15R_c$  in the  $x$ ,  $y$ , and  $z$  directions. Hence, at the edges of the AIKEF simulation domain, the electromagnetic fields have returned to their background values. However, although an energetic particle may reach this region of uniform fields and travel outside of the volume represented by the AIKEF domain, gyration about the magnetospheric field (see Table 2) and/or bounce along the field and subsequent mirroring (along with the associated magnetospheric drifts) may allow the backtraced particle to return close to the moon where it would again be exposed to perturbed electromagnetic fields, potentially intersecting the exobase and becoming forbidden. Indeed, as illustrated by Liuzzo et al. (2019a), these effects play an important role in the understanding of energetic particle precipitation onto Callisto. We must therefore consider the gyration, bounce, and drift motions of the particle during its excursion outside of the AIKEF simulation domain while located far from the moon.

To represent the motion of an energetic particle along a magnetospheric field line during its half-bounce period (i.e., the time it takes a particle to travel from Callisto, to its mirror point near one of Jupiter's poles, and back), we apply the approach of Roederer (1967). Given a particle's (equatorial) pitch angle and energy, this method calculates the displacement of the particle's guiding center  $\rho$  in the azimuthal (i.e., corotation) direction after a half-bounce period associated with the gradient, curvature, and  $\mathbf{E} \times \mathbf{B}$  drifts as a particle travels through magnetospheric fields. Within the GENTOO model, this azimuthal displacement  $r_{eq}$  therefore represents how far an ion or electron has traveled along the azimuthal (i.e.,  $\hat{\mathbf{x}}$ ) direction after completing a half-bounce and returning near the moon. In order to consider the particle's bounce motion throughout the magnetosphere (i.e., while outside of the AIKEF domain), we represent the Jovian magnetospheric field lines using the *same* combination of the Khurana (1997) model for the Jovian current sheet and the VIP4 internal field model (Connerney et al., 1998) that was applied to calculate the background field vectors for the AIKEF simulations. Such an approach is necessary for particle tracing, since an important requirement is the continuity of magnetic field lines across the boundary where the hybrid simulation domain connects to the global magnetospheric field line model. If the field lines were discontinuous, particle trajectories across these boundaries may experience an artificial deflection due to the sudden change of the magnetic field vector. However, the magnetic field perturbations vanish well within the boundary of the AIKEF simulations (i.e., the fields return to their background values; see Figures 1 and 2). Therefore, by calculating the background vector for the local AIKEF model from the global magnetospheric field model, we preclude the occurrence of discontinuities at planes where both models meet. We note, however, that the global magnetospheric field models do not include contributions from magnetopause currents, which may slightly alter the trajectories of particles that come close to the magnetopause during their bounce (see, e.g., Figure 2c of Liuzzo et al., 2019a), or particle depletion at high Jovian latitudes within the loss cone.

In order to apply the approach of Roederer (1967) to represent the azimuthal displacement of a particle during its bounce, we must first calculate the location of its guiding center  $\rho$  (given the particle's position  $\mathbf{r}$ ) as it exits the AIKEF simulation domain. For the energies considered in this study, ions are non-relativistic with  $\gamma < 1.01$ , so their gyromotion can be described as a circle since there is no relativistic length contraction along the direction of the  $\mathbf{E} \times \mathbf{B}$  drift velocity (see Friedman & Semon, 2005; Takeuchi, 2002). Hence, the vector  $\mathbf{G}$  from an ion's position  $\mathbf{r}$  to its guiding center  $\rho$  is given by:

$$\mathbf{G} = r_g \cdot \frac{\mathbf{v}^* \times \mathbf{B}}{|\mathbf{v}^* \times \mathbf{B}|}, \quad (1)$$

where  $\mathbf{v}^* = \mathbf{v} - \mathbf{v}_{\mathbf{E} \times \mathbf{B}}$ , where  $\mathbf{v}$  is the particle's velocity and  $\mathbf{v}_{\mathbf{E} \times \mathbf{B}} = \mathbf{E} \times \mathbf{B}/B^2$  denotes the  $\mathbf{E} \times \mathbf{B}$  drift velocity. Equation 1 can be rewritten using the pitch angle  $\alpha$  of the ion with respect to the local magnetic field

$$\mathbf{G} = r_g \cdot \frac{\mathbf{v}^* \times \mathbf{B}}{|\mathbf{v}^*||\mathbf{B}| \sin(\alpha)} = r_g \cdot \frac{\mathbf{v}^* \times \mathbf{B}}{|\mathbf{v}_\perp^*||\mathbf{B}|}, \quad (2)$$

with velocity  $\mathbf{v}_\perp^*$  perpendicular to the direction of the magnetic field. Considering the ion's gyroradius  $r_g = |\mathbf{v}_\perp^*|/\Omega$ , Equation 2 simplifies to

$$\mathbf{G} = \frac{\mathbf{v}^* \times \mathbf{b}}{\Omega}, \quad (3)$$

given the particle's gyrofrequency  $\Omega = q|\mathbf{B}|/m$  and defining the unit vector along the magnetic field  $\mathbf{b} = \mathbf{B}/|\mathbf{B}|$ . Hence, for an ion located at position  $\mathbf{r}$  prior to “bouncing” (i.e., immediately before it exits the AIKEF simulation domain along the direction parallel/antiparallel to the magnetospheric field), the location of its guiding center  $\boldsymbol{\rho}$  is given by  $\boldsymbol{\rho} = \mathbf{r} + \mathbf{G}$ . With  $\boldsymbol{\rho}$ , we are able to calculate the azimuthal displacement  $r_{eq}$  of the particle's guiding center after bouncing through the magnetospheric fields and returning near the moon's orbit. After bouncing, the new location of the guiding center for a particle traced forward in time is given by  $\boldsymbol{\rho}' = \boldsymbol{\rho} + r_{eq}\hat{\mathbf{x}}$ , with primed quantities denoting the value *after* the particle has traveled through the magnetosphere and returned near the moon. For ions,  $r_{eq} > 0$  since the direction of the gradient-curvature drift is aligned with the direction of the  $\mathbf{E} \times \mathbf{B}$  drift; hence, a *backtraced* ion is always displaced toward upstream after returning from a bounce.

The approach of Roederer (1967) does not include any information regarding the *phase* of a particle's gyration about its guiding center after completing a half bounce. However, the *gyrophase* at which an ion returns near Callisto after bouncing may be affected by multiple effects as they travel through the magnetosphere. For example, parallel electric fields within the high-latitude auroral regions of Jupiter or other Alfvénically driven stochastic effects may accelerate particles as they encounter this region (e.g., Saur et al., 2018), and various wave-particle interactions may scatter or otherwise modify the pitch angles of energetic particles during their bounce motion (e.g., Menietti et al., 2012; Shprits et al., 2018). Yet, because the gyroradii of ions in the ambient magnetospheric fields near Callisto already exceed the moon's radius at energies  $E \gtrsim 10$  keV, an ion's gyrophase may indeed influence whether or not it hits Callisto's atmosphere or gyrates around the moon. If an ion returns close enough after bouncing (i.e., with  $r_{eq} \approx r_g \approx R_C$ ), the gyrophase at which it is re-inserted into the AIKEF domain may therefore determine whether the trajectory is considered allowed or forbidden. To address these uncertainties, we re-inject ions into the AIKEF domain after bouncing using a randomized perpendicular velocity vector (i.e., at a random gyrophase with its position  $\mathbf{r}'$  after bouncing located anywhere on the circle defined by  $\boldsymbol{\rho}'$  and  $\mathbf{G}'$ , such that  $|\mathbf{v}'_{\perp}| = |\mathbf{v}^*_{\perp}|$ ), with their parallel velocity reversed (i.e.,  $\mathbf{v}'_{\parallel} = -\mathbf{v}_{\parallel}$ ).

Besides their bounce motion, energetic ions may leave Callisto's immediate environment through gyration due to the sheer size of their gyroradii. As illustrated in Table 2, the gyroradius of a doubly charged, 11.8 MeV oxygen ion may exceed  $r_g > 100R_C$  within the center of the Jovian current sheet (where  $|\mathbf{B}|$  minimizes). Hence, although its gyromotion may carry it far from Callisto, an ion may still re-encounter the moon's local environment after completing only a single gyration (see also Figure 4 of Regoli et al., 2016). Therefore, if an energetic ion gyrates outside of the hybrid simulation domain, we set the electromagnetic fields to their background values used for the simulations (see Table 1) and allow the particle to continue its gyration and drift motions through these uniform fields to prevent the particle from bouncing prematurely. When it re-enters the AIKEF domain, the ion's motion is again calculated using the perturbed fields. Particles are only allowed to bounce after traveling a distance along the direction of the background magnetic field that exceeds the length of the diagonal of the AIKEF domain. This ensures that the particle will no longer be located within the AIKEF domain where it may otherwise interact with the perturbed fields. After satisfying this condition, we calculate the particle's azimuthal displacement  $r_{eq}$  (from its given energy and pitch angle) and re-inject it into the AIKEF domain where it may potentially re-encounter Callisto's locally perturbed electromagnetic environment.

In contrast to ions, the gyroradii of electrons do not greatly exceed the size of Callisto (see Table 2). At the lowest energies in this study (below  $E \lesssim 0.5$  MeV), electron gyroradii remain at values  $r_g \ll R_C$ . Hence, the gyrophase of an electron at these low energies does *not* need to be randomized since it does not affect whether its trajectory is forbidden: its small gyroradius precludes the electron from gyrating around Callisto. However, the gyroradii of the highest energy electrons considered in this study ( $E > 0.5$  MeV) approach the size of the moon, for pitch angles of  $\alpha \approx 90^\circ$ . At these energies, electrons are relativistic (for a 0.5 MeV electron,  $\gamma \approx 2$ ; see Table 2); due to the non-linearity of the relativistic equation of motion in velocity, the contribution of the  $\mathbf{E} \times \mathbf{B}$  drift to an electron's gyromotion is not separable from the total velocity (see Takeuchi, 2002). In addition, the trajectory of a relativistic electron in the rest frame of its guiding center is an ellipse, due to the relativistic length contraction along the  $\mathbf{E} \times \mathbf{B}$  direction.

As a result, the above Equations 1–3, which assume a circular trajectory for particle gyration, are no longer applicable for these high-energy electrons in the same way as described above for non-relativistic ions. It is

therefore not feasible to randomize the phase of these electrons' gyration, and instead re-inject electrons at an identical gyrophase (i.e., an identical perpendicular velocity) after bouncing, with their parallel velocity reversed (for further details, see Liuzzo et al., 2019a, 2020). For this reason, we displace the electron's position  $\mathbf{r}$  in the  $\hat{\mathbf{x}}$  direction by an azimuthal value of  $r_{eq}$  after bouncing, *not* the position of its guiding center  $\rho$ . We note that the abundance of electrons at energies  $E > 1.5$  MeV is more than 5 orders of magnitude lower than the abundance of the lower-energy electrons (at energies  $E < 10$  keV; see Section 3.2), any uncertainty in a high-energy electron's gyrophase after bouncing only affects the overall electron fluxes in a minor, quantitative way.

Importantly, unlike the case of energetic ions, the charge-dependence of the gradient-curvature drift results in a critical energy  $E_c$  for electrons ( $\approx 1$  MeV near Callisto; see Liuzzo et al., 2019a) at which  $\mathbf{v}_{E \times B}$  exactly cancels the electron's gradient-curvature drift velocity (see also Khurana et al., 2008; Krupp et al., 2013). At energies  $E < E_c$ , the net drift motion therefore results in an electron that is traced forward in time traveling along the corotation direction during its half-bounce period (i.e.,  $r_{eq} > 0$ ); a *backtraced* electron is therefore displaced toward upstream with respect to the corotating flow. At energies  $E > E_c$ , however, a forward-traced electron travels against the direction of corotation (toward upstream;  $r_{eq} < 0$ ), so electrons traced *backward* in time within the GENTOo framework are displaced toward downstream.

The trajectory of an energetic ion or electron is only finally considered allowed once it is far enough from Callisto that it could not re-encounter the moon. For backtraced *ions*, this condition is reached when the azimuthal component of its guiding center position  $\rho$ , plus the ion's gyroradius, is located farther upstream of Callisto than the upstream face of the AIKEF domain; that is,  $\rho_x + r_g < -15R_C$  (note that  $\rho_x < 0$  for a particle located upstream of Callisto). This conservative limit ensures that an ion could not re-encounter Callisto's perturbed field region. For backtraced *electrons*, trajectories are allowed when the azimuthal component of the electron's position  $\mathbf{r}$  is either located farther upstream than the upstream face of the AIKEF box (i.e.,  $r_x < -15R_C$  for energies  $E < E_c$ ), or located farther downstream than the downstream face of the AIKEF box ( $r_x > +15R_C$  for  $E > E_c$ ). Note that even for the highest energy considered in this study, the gyroradius of an electron with pitch angle  $\alpha = 90^\circ$  remains  $r_g \lesssim 4R_C$ ; therefore, electrons cannot re-encounter Callisto's perturbed electromagnetic environment through gyration alone when located beyond the downstream face of the simulation domain.

### 3.2. Calculating Energetic Particle Fluxes Onto Callisto's Atmosphere

In order to convert each allowed trajectory into a particle flux onto Callisto's atmosphere, we require information on the distribution of the energetic magnetospheric particles in the moon's local magnetospheric environment. Figure 3 displays the differential flux  $J_0$  for energetic ions and electrons in the Jovian magnetosphere near Callisto's orbit. The green, blue, and yellow lines correspond to the energetic hydrogen, oxygen, and sulfur populations, respectively, as provided in Mauk et al. (2004). These curves were fit to Galileo Energetic Particle Detector (EPD) ion data obtained from a magnetospheric sheet crossing during the G8 orbit (the "G8\_PS/A" fit in Table 1 of Mauk et al., 2004), at a time when the spacecraft was near the center of the magnetospheric current sheet and located at a radial distance of  $25.17R_J$  from Jupiter. Since Galileo was near Callisto's orbital position but far from the moon itself, this data set is unaltered by the presence of Callisto or its interaction with the magnetospheric plasma and represents the ambient population of energetic ions to which the moon was exposed, assuming that the properties of this population do not strongly vary along the direction of Callisto's orbit. Due to uncertainties associated with determining the count rates of ions entering the various EPD channels, Mauk et al. (2004) provide fits over slightly disparate energy ranges for each species: for hydrogen at energies  $E$  in the range of  $22 \text{ keV} \leq E \leq 32 \text{ MeV}$ , oxygen from  $45 \text{ keV} \leq E \leq 9 \text{ MeV}$ , and sulfur between  $82 \text{ keV} \leq E \leq 10 \text{ MeV}$  (solid lines). For this study, we will focus on particles within the energy range of  $4.5 \text{ keV} \leq E \leq 11.8 \text{ MeV}$ . Since this range extends slightly beyond that presented in Mauk et al. (2004), dashed lines in the figure denote the energies at which these fits are extrapolated (see also Poppe et al., 2018).

The orange line in Figure 3 displays the differential number flux of energetic electrons near Callisto. To obtain this fit, we use the Galileo Interim Radiation Electron (GIRE) model (Garrett et al., 2003), which applies data from the Galileo, Pioneer, and Voyager missions to estimate the energetic electron environment within the Jovian magnetosphere. Since this model is not valid below energies of  $E \lesssim 20$  keV (see, e.g., the discussion in de Soria-Santacruz et al., 2016), we apply a separate kappa distribution to fit the lower-energy electron population as discussed in Jun et al. (2019), using a kappa factor of 1.1 and a characteristic energy of 200 eV. To ensure that

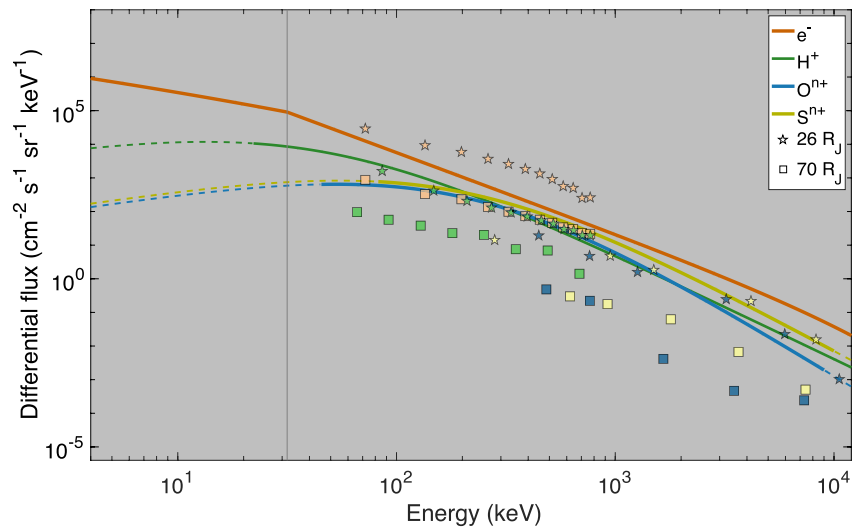


**Figure 3.** Differential flux of energetic ions and electrons in the undisturbed plasma near Callisto's orbit. The curves represent empirical models of the differential particle fluxes near an M-shell of 26 (i.e., with Callisto located within the Jovian magnetospheric current sheet): fits for energetic (green) hydrogen (blue) oxygen, and (yellow) sulfur are obtained using the values provided in Mauk et al. (2004), while the curve for (orange) electrons is obtained using either the Galileo Interim Radiation Electron model (Garrett et al., 2003) at energies  $E \geq 31.6$  keV or a kappa distribution for energies  $E < 31.6$  keV (see Jun et al., 2019). For ions, dashed lines represent energies that extend beyond the range for which the data were obtained. Individual points correspond to measurements obtained during the Juno mission, at times when the spacecraft was located within Jupiter's magnetic equator near an orbital distance of (stars)  $26R_J$  or (squares)  $70R_J$  from the planet. See text for further detail.

the curve for electron differential fluxes is continuous at all energies considered, we transition between these two fits where their curves overlap at  $E = 31.6$  keV.

In addition to the fits, Figure 3 also includes measurements of the energetic ion and electron differential flux as obtained from select encounters during the Juno missions. The stars included in Figure 3 represent the ambient energetic particle distribution near Callisto's orbital position (i.e., near a radial distance to Jupiter of  $26R_J$ ). To obtain these points, we averaged the measurements from the Jupiter Energetic Particle Detector Instrument (JEDI; Mauk et al., 2017) instrument onboard Juno when embedded within the Jovian magnetospheric current sheet. The orange stars correspond to electron fluxes as obtained from JEDI, while the green, blue, and yellow stars visible in Figure 3 correspond to the differential fluxes of energetic protons, oxygen, and sulfur ions, respectively. For electrons and protons, these measurements were taken during the PJ34 orbit of Jupiter, between 18:00 and 19:00 on 19 July 2021. For the oxygen and sulfur ions, these measurements were obtained during the PJ15 orbit, from 13:00 to 14:00 on 5 September 2018. At these times, the spacecraft was within the Jovian current sheet near an M-shell of 26 but located far from Callisto and was therefore unaffected by the moon's local plasma interaction. For further details on the fitting procedure for JEDI data, the reader is referred to, for example, Paranicas et al. (2021, 2022).

Paranicas et al. (2018) have shown that over a full synodic rotation, the tilt of Jupiter's magnetic axis causes the magnetospheric field lines to which Callisto is connected to be highly variable. These authors investigated field lines that pass through the Jovian magnetic equator as a function of “magnetic distance” to Jupiter—defined as the radial distance from Jupiter to the point of minimum magnetic field intensity on the field line to which a moon is connected (see also Paranicas et al., 2018). In doing so, they found that the field lines near Callisto range in magnetic distances from  $26.3R_J$  (when Callisto is near the Jovian magnetic equator) to beyond  $70R_J$  (when the moon is far from the equator). This occurs because when Callisto is located at high magnetic latitudes, the magnetospheric field lines near the moon have a strong radial component; however, the point on the field line where  $|B|$  is minimized—i.e., where the field line “turns around” and is mainly pointed southward—is located far beyond the orbit of the moon (see, e.g., Figure 2c of Liuzzo et al., 2019a). Paranicas et al. (2018) have shown that the energetic proton population at Callisto's orbital position varies by approximately an order of magnitude for these two magnetic distances. Although these authors did not constrain the variability in the electron, oxygen, and

sulfur populations with magnetic distance, their findings are consistent with Kollmann et al. (2018), who found a similar order of magnitude difference for  $E > 35$  keV electrons,  $E = 780$  keV protons, and  $E = 580$  keV oxygen ions between M-shells of 26.3 and 70 as measured by the Galileo EPD.

To highlight the variability in each of the energetic particle species near the moon over a synodic period over the energy range relevant to this study, the squares in Figure 3 correspond to JEDI measurements when Juno was located within Jupiter's magnetic equator, but near a distance of  $70R_J$  from the planet. These observations therefore likely represent the differential fluxes of energetic particles near Callisto when the moon is located at maximum distances from the Jovian magnetic equator. The electron observations were obtained during the PJ15 encounter on 31 August 2018 between 02:00 and 02:30, while the ion observations were taken during the PJ08 encounter on 25 August 2017 from 19:40–21:40. Note that we have excluded particles with local pitch angles measured by Juno from  $70^\circ < \alpha < 110^\circ$ , since particles with predominantly perpendicular velocities likely mirror in the magnetospheric fields prior to reaching the Jovian rotational equator near Callisto's orbital position at  $26.3R_J$ . As visible in Figure 3, the energetic proton, oxygen, and electron differential fluxes obtained by Juno within the Jovian current sheet (stars) are indeed over an order of magnitude larger than the fluxes obtained by Galileo when located far above the center of the sheet (squares) at nearly every energy. Figure 3 also illustrates that the Juno electron fluxes obtained within the sheet near Callisto's orbital position (stars in the figure) are  $\sim 2$ – $4$  times larger than the intensities predicted by the kappa distribution and the GIRE model near an M-shell of 26. The measured Juno ion fluxes, on the other hand, closely match those predicted by the fits from Mauk et al. (2004) when Galileo was within the magnetospheric current sheet.

The curves presented in Figure 3 are representative of the energetic particle environment near Callisto when the moon is located near the center of the Jovian current sheet (i.e., near an M-shell of 26). In order to isolate the effect of the electromagnetic perturbations in Callisto's local environment on energetic particle dynamics, this study will use these four curves to calculate the energetic electron and ion fluxes onto the moon. However, for part of a synodic period, Callisto is connected to magnetospheric field lines that cross the Jovian magnetic equator at distances beyond  $70R_J$  where the differential fluxes of the energetic particles are reduced by at least an order of magnitude. A brief discussion on the sensitivity of our results to a lower abundance of energetic particles far from the center of the Jovian magnetospheric current sheet is presented in Section 5. We note that since the Juno measurements are obtained during only represent the abundances at only a single snapshot in time, a complete investigation on the effect that the variability in the ambient energetic particle distributions *themselves* have on the resulting fluxes would require additional measurements to constrain the ambient particle populations (e.g., using Juno measurements from multiple encounters, perhaps combined with data from the Galileo mission or the upcoming JUPITER ICY moons Explorer mission).

To convert the allowed particle trajectories into fluxes onto the moon's atmosphere, we assume that the ambient electron and ion pitch angle distributions are isotropic in the plasma near Callisto. Nénon et al. (2022) have recently shown this approximation to be valid for electrons above energies of 1 MeV near this moon, and observations of energetic ions by the Galileo EPD are roughly isotropic at Callisto's orbital position (Mauk et al., 2004). At Europa, anisotropies in the magnetospheric energetic ion distribution only affect the resulting fluxes onto the moon quantitatively, reducing the total flux by approximately 10% (Addison et al., 2021). Hence, any potential anisotropies in the distributions near Callisto will likely not play a strong role on the resulting fluxes onto the moon's exobase. Since the integration time of the energetic particle observations is similar to the time it takes a spacecraft to travel through a region that is the size of the AIKEF domain (i.e.,  $\sim 30R_C$ ), we assume that the distribution of the energetic ions and electrons remains unchanged in Callisto's local environment. The phase space density  $f_0(p_0)$  represented by any backtraced particle that reaches the unperturbed ambient plasma can then be obtained based on its momentum  $p_0 = \gamma m |\mathbf{v}_0|$  as it exits Callisto's local environment using the relation  $f_0 = J_0 / p_0^2$  (where  $m$  is the particle's rest mass,  $\mathbf{v}_0$  is the particle's velocity in the ambient magnetospheric plasma, and  $J_0$  is the ambient differential particle flux as shown in Figure 3). In the absence of collisions (i.e., for particles that remain at altitudes above the exobase), we can apply Liouville's theorem to obtain the momentum distribution function at the top of Callisto's atmosphere  $f(p)$ . Taking moments of this distribution function provides the particle flux onto the top of the atmosphere (for further information, see also, e.g., Kollmann et al., 2018; Liuzzo et al., 2020; Xiao et al., 2008). Again, note that below the exobase where Callisto's atmosphere is collisional (Carberry Mogan et al., 2021; Cunningham et al., 2015), application of Liouville's theorem is no longer a valid approach to describe the particles' dynamics. Using GENTOO to calculate particle fluxes at altitudes below the starting grid would lead to inaccurate results since the approach is unable to capture, for example, the attenuation

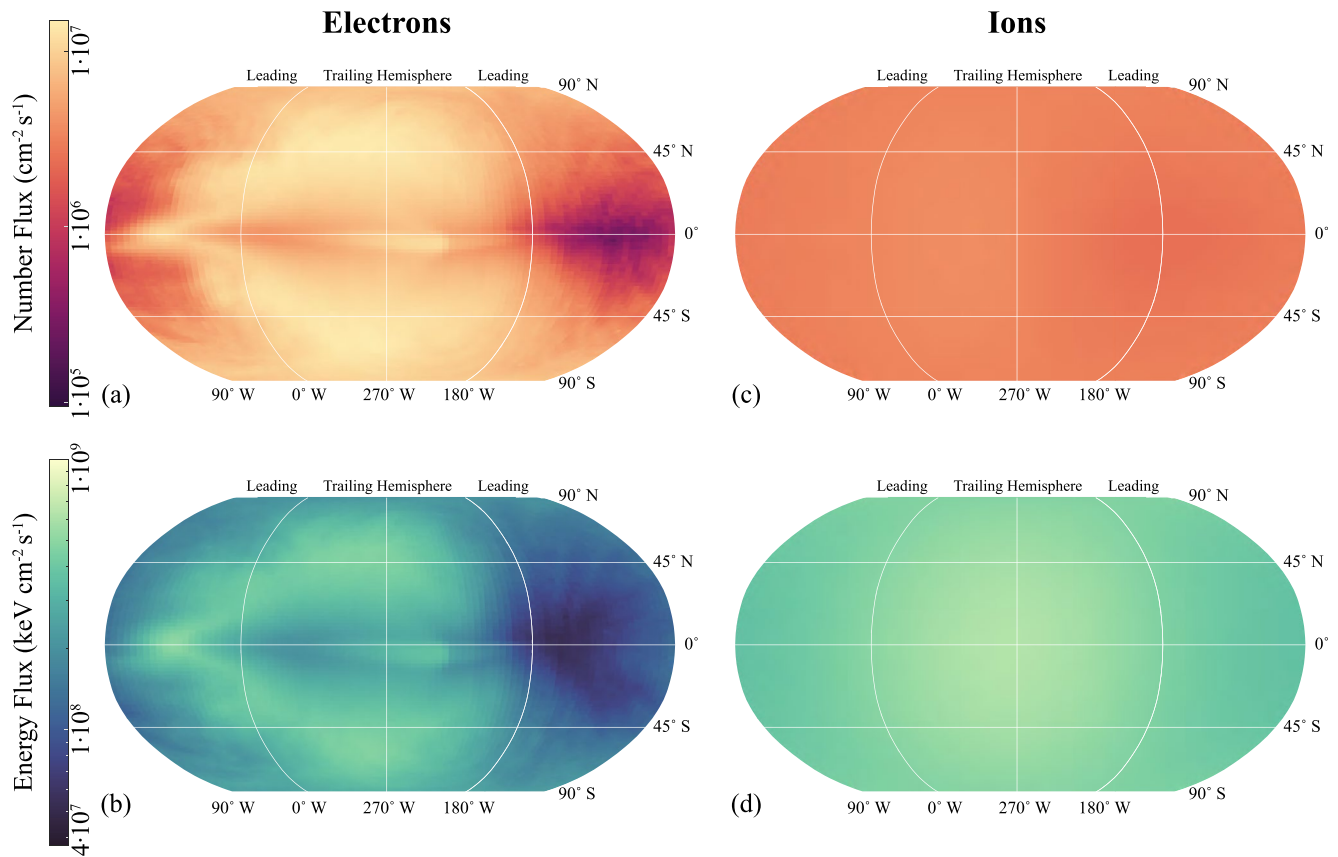


**Figure 4.** Energetic (left column; a–b) electron and (right column; c–d) ion (top row) number and (bottom row) energy fluxes onto the top of Callisto's atmosphere (at  $1.1R_C$ ) when the moon is located near the center of the Jovian magnetospheric current sheet. Ion fluxes include the contribution from all three species investigated: hydrogen, oxygen, and sulfur. West Longitude is used for each map, with  $0^\circ\text{W}$  located within the sub-Jovian hemisphere and  $90^\circ\text{W}$  located in Callisto's orbital leading (i.e., wakeside) hemisphere, as denoted at the top of each panel.

of a particle's energy associated with its interaction with Callisto's atmosphere that occurs below the exobase. This effect is beyond the scope of this current investigation and such a study is left for future work.

## 4. Energetic Particle Fluxes Onto Callisto's Atmosphere

### 4.1. Callisto Embedded Within the Jovian Current Sheet

Figure 4 displays maps of the energetic particle fluxes onto the top of Callisto's atmosphere when located near the center of Jupiter's magnetospheric current sheet. The left and right columns show the electron and total ion fluxes (i.e., the sum of the hydrogen, oxygen, and sulfur fluxes), respectively; the top row of Figure 4 displays the number flux while the bottom row shows the energy flux. While the number flux is useful to determine those locations where the most particles precipitate onto the atmosphere, the energy flux can be applied to understand, for example, the locations where enhanced energy transport from the magnetosphere into the atmosphere occurs, or the alteration of the surface (e.g., Dalton et al., 2013). The vertical axis in each panel displays latitude, with  $90^\circ\text{N}$  corresponding to Callisto's north pole,  $0^\circ$  to the equator, and  $90^\circ\text{S}$  to the south pole of the moon. West longitude is displayed on the horizontal axis of each panel, in which  $0^\circ\text{W}$  is located within Callisto's sub-Jovian hemisphere,  $90^\circ\text{W}$  is in the orbital leading (i.e., wakeside) hemisphere,  $180^\circ\text{W}$  is located within the moon's anti-Jovian hemisphere, while  $270^\circ\text{W}$  is located in the moon's trailing hemisphere.

The average energetic electron number flux onto the top of Callisto's atmosphere is  $7.3 \cdot 10^6 \text{ cm}^{-2} \text{ s}^{-1}$ , with an average energy flux of  $2.2 \cdot 10^8 \text{ keV cm}^{-2} \text{ s}^{-1}$ . By integrating the curve for the differential electron fluxes in Figure 3 over the energy range used for this study, these fluxes can be compared to a (hypothetical) case without any plasma interaction effects where electrons of all energies deposited their flux onto Callisto uniformly. In



doing so, the number flux onto the exobase for this hypothetical case would reach  $3.8 \cdot 10^8 \text{ cm}^{-2} \text{ s}^{-1}$ ; hence, when located near the center of the magnetospheric current sheet, Callisto's plasma interaction reduces the averaged electron flux onto the moon's exobase by nearly two orders of magnitude.

Figure 4a illustrates that the electron fluxes display a noticeable leading/trailing asymmetry to the electron fluxes. This is characterized by a region of high fluxes in Callisto's orbital trailing hemisphere reaching number fluxes up to  $1.5 \cdot 10^7 \text{ cm}^{-2} \text{ s}^{-1}$ , that is, a factor of 2 larger than the global average. These regions of enhanced electron flux in the trailing hemisphere extend to high latitudes, forming a “lens” nearly centered around the trailing apex, similar to those seen at, for example, the icy moons of Saturn (e.g., Paranicas et al., 2014). In addition, within this lens are areas of lower flux closer to the equatorial region that is likely associated with electrons moving along the field lines and precipitating onto the moon at higher latitudes before accessing more equatorial locations. Within the anti-Jovian, leading hemisphere, number fluxes are reduced, dropping nearly two orders of magnitude below the average, to values of  $2.4 \cdot 10^5 \text{ cm}^{-2} \text{ s}^{-1}$ . A similar lens feature is not visible within the leading hemisphere. Although electrons at energies  $E \gtrsim 1 \text{ MeV}$  are able to travel against the corotation direction (i.e., from the leading hemisphere toward the trailing hemisphere), the abundance of these highest energy electrons in the ambient plasma near Callisto is too low to noticeably contribute to the flux pattern deposited onto the moon's exobase (see Figure 3).

In addition to the global leading/trailing asymmetry in the patterns, the fluxes within the sub- and anti-Jovian hemispheres are themselves asymmetric and non-uniform, since the energetic electrons are strongly affected by Callisto's perturbed electromagnetic environment (see also Liuzzo et al., 2019a). The most notable fine-scale feature is visible in Callisto's leading, sub-Jovian hemisphere. Starting at  $0^\circ$  W longitude, beyond the “lens” region in the trailing hemisphere near latitudes of  $\sim 45^\circ\text{N}$  and  $\sim 45^\circ\text{S}$ , a region of enhanced electron flux comes to a point near Callisto's wakeside apex. Beginning as two high-flux regions, these enhancements are focused toward more equatorial latitudes when traveling westward into the moon's leading hemisphere, thereby forming a “wedge-like” pattern around the equator in the leading, sub-Jovian hemisphere. An analogous feature does *not* appear in Callisto's leading, anti-Jovian hemisphere: instead, the equatorial electron fluxes reach their minimum values between  $90^\circ\text{W}$  and  $180^\circ\text{W}$  longitude.

To understand the cause of this longitudinal asymmetry that occurs between the sub- and anti-Jovian hemispheres on the moon's leading side, Figure 5 displays the path of a single 4.5 keV electron with an allowed trajectory as it traveled through Callisto's perturbed electromagnetic field environment. This trajectory is color-coded to represent the magnetic field magnitude to which the electron is exposed along its path. The vantage point in panel 5a is from a location in the upstream, sub-Jovian hemisphere, while panel 5b is viewed from the other side of Callisto; that is, within the downstream, anti-Jovian hemisphere. The red dot in each panel indicates the particle's position where it impacted Callisto's exobase near  $45^\circ\text{W}$  longitude at a position  $(x, y, z) = (0.78, 0.78, 0.00) R_C$ . Hence, this particle contributes to the near-equatorial region of high electron flux in Callisto's sub-Jovian leading hemisphere, at the tip of the “wedge” near the moon's leading apex, as visible in Figure 4a. Annotations in panel 5a denote when the electron either (*R*) returned near Callisto within the perturbed electromagnetic fields or (*E*) exited the moon's local environment to begin its bounce. The number denotes the amount of times that the electron has traveled through Callisto's perturbed electromagnetic environment during that particular segment of its trajectory. Note that in total, this particular electron bounced through and mirrored in the Jovian magnetospheric fields multiple times upstream of Callisto before it encountered the moon's perturbed electromagnetic environment; only the final portion of its trajectory (with  $x > -2R_C$ ) is shown in Figure 5.

On its first pass through Callisto's electromagnetic environment (denoted R1 in panel 5a), this electron approaches the moon from upstream in the northern hemisphere. At distances approximately  $1.5R_C$  above the moon's surface, the electron encounters the magnetic field enhancement above the north pole associated with the strongly draped field ( $|\mathbf{B}| \approx 5|\mathbf{B}_0|$ ; see Figure 1e), which prevents this particle from reaching the polar hemisphere. Instead, the electron mirrors in the locally enhanced field, causing the particle to travel northward away from Callisto as it exits the perturbed electromagnetic environment (E1 in the figure). As the electron bounces through the Jovian magnetosphere, mirroring at high (Jovian) latitudes, and returns near Callisto, it is displaced azimuthally by approximately  $r_{eq} \approx 2.5R_C$  toward the moon's downstream hemisphere. Hence, the electron re-enters the perturbed electromagnetic environment, as denoted by the red arrow marked R2 in Figure 5a.

During this second pass through Callisto's perturbed environment, the electron's dynamics are again strongly affected by the electromagnetic fields. The electron approaches the moon from the north and experiences an

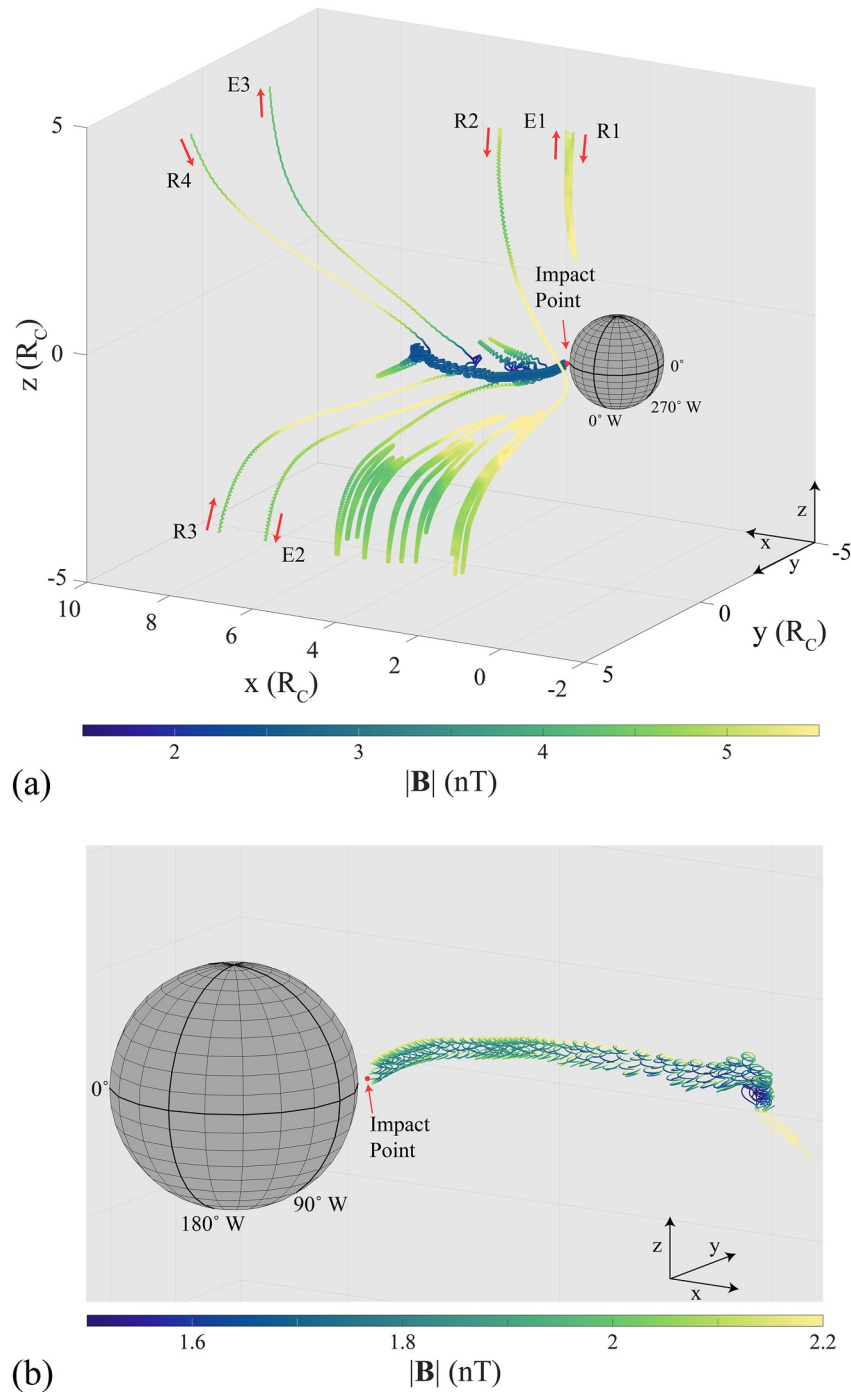


**Figure 5.** Trajectory of a single, 4.5 keV electron with an allowed trajectory as it travels through Callisto's perturbed electromagnetic environment. The trajectory is color-coded with the value of the local magnetic field magnitude to which the electron is exposed; note the different color scales used for the two panels. The vantage point of panel (a) is a location upstream of Callisto in the sub-Jovian hemisphere, while panel (b) is viewed from Callisto's wakeside, anti-Jovian hemisphere. Note that panel (b) only shows the final portion of the electron's trajectory, while it was confined to the thin sheet of reduced magnetic field located in the downstream, sub-Jovian hemisphere of Callisto (see also Figure 2e). Annotations in (a) denote when the electron (*R*) returned to or (*E*) exited Callisto's local environment, with the number indicating the number of times the electron has passed through the perturbed fields during that segment of its trajectory. See text for further detail.

enhanced magnetic field magnitude as it travels through the sub-Jovian hemisphere. After passing the moon, the electron experiences an inhomogeneity in the magnetic field south of the moon that causes the particle to locally mirror multiple times, all the while drifting toward downstream along the corotation direction, before it finally exits the perturbed fields southward along a magnetic field line (E2). After again bouncing through the magnetospheric fields and returning  $\sim 2.5R_C$  farther downstream due to its drift (point R3), the electron again travels through the perturbed fields, encountering the region of reduced magnetic field in Callisto's wakeside, before exiting to the north of the moon.

On its final return near Callisto (point R4), Figure 5a illustrates that the electron's azimuthal drift motion has carried it  $10R_C$  downstream of the moon. However, the draped fields channel the particle back toward Callisto, where it enters the thin sheet where the local magnetic field is reduced to less than half the background value ( $|\mathbf{B}| \approx 1.5$  nT compared to  $|\mathbf{B}_0| = 4$  nT; see also Figures 1e and 2e). This is further illustrated in panel 5b, which highlights the final segment of this electron's trajectory before impacting Callisto's exobase. When trying to escape this thin sheet of reduced magnetic field to the north or to the south, the electron experiences a rapid spatial increase in  $|\mathbf{B}|$ . This increase, combined with the electron's nearly perpendicular pitch angle, causes the particle to mirror and reverse its direction of travel. The electron therefore becomes quasi-trapped between the two magnetic lobes where the field is enhanced (see Figure 1e). All the while, the electron, located along the  $+\hat{y}$  edge of the region of reduced magnetic field downstream of Callisto (see Figure 2e) is able to "swim upstream" toward the moon's leading, sub-Jovian hemisphere. Since the gradient of the magnetic field within this region has a strong component along the  $+\hat{y}$  direction and the magnetic field vector is mainly along  $-\hat{z}$ , the electron's gradient drift velocity ( $\mathbf{v}_\nabla \propto \mathbf{B} \times \nabla B/q$ ) points along the  $-\hat{x}$  direction (i.e., toward upstream for a negatively charged electron), thereby allowing the particle to travel toward the moon. Traveling upstream along the edge of the magnetic neutral sheet (dark blue colors downstream of Callisto in Figure 2e), the electron experiences a mirror force that prevents it from crossing into the region of enhanced magnetic field (yellow colors visible in Figure 2e). Therefore, as the electron approaches Callisto, it is funneled along the  $-\hat{y}$  direction toward the moon's leading, sub-Jovian hemisphere (see also Figure 5), where it precipitates onto the exobase. Hence, the perturbed electromagnetic environment in general, and the draped fields and associated downstream sheet of reduced magnetic field in particular, funnel these electrons toward Callisto's orbital leading hemisphere.

Although Callisto's interaction with the thermal magnetospheric plasma generates regions of enhanced energetic electron flux in Callisto's leading, sub-Jovian hemisphere, it creates regions of *reduced* flux in the leading, anti-Jovian hemisphere. The large gyroradii of the ionospheric pickup species (see Figure 2h) drag the magnetic field pileup region along the direction of the convective electric field  $\mathbf{E}_0$  into the anti-Jovian hemisphere and partially extend it into the leading hemisphere (see Figure 2e). This enhanced magnetic field acts as a barrier to energetic electrons, deflecting them away from the moon and preventing their access to these regions of Callisto (as was also visible in the behavior of the electron in Figure 5a when it encountered the draped field lines).

In addition to the energetic electron fluxes, Figure 4 also includes the energetic ion fluxes onto Callisto. Averaged across the atmosphere, the ion number flux is nearly a factor of 2 lower than the average electron flux for this scenario ( $3.2 \cdot 10^6$  cm $^{-2}$  s $^{-1}$  for ions, compared to  $5.9 \cdot 10^6$  cm $^{-2}$  s $^{-1}$  for the electrons), as also expected from the ambient differential fluxes near Callisto (see Figure 3). In contrast to the electrons, Callisto's plasma interaction only reduces the averaged ion flux by a factor of  $\sim 5$ , compared to the hypothetical scenario of uniform fluxes globally without any plasma currents: integrating the ion curves in Figure 3 yields a combined number flux of  $1.7 \cdot 10^7$  cm $^{-2}$  s $^{-1}$ . The average ion energy flux is even 1.5 times *larger* than the electron energy flux, reaching an average value of  $4.8 \cdot 10^8$  keV cm $^{-2}$  s $^{-1}$ . Compared to the electron fluxes in Figure 4, the ion fluxes are nearly homogeneous across the exobase with only the slightest deviation from these averaged values, with little-to-no fine-structure visible. Rather, the region of minimum ion flux located in the anti-Jovian hemisphere near 180° W longitude (see also Figure 6) receives only approximately two-thirds of the flux deposited into the antipodal hemisphere (between 270°W and 90°W) where the maximum energetic ion flux occurs.

To better understand the contribution of the three ion species to the total ion flux, Figure 6 shows the number and energy fluxes of energetic protons, oxygen, and sulfur ions individually. Protons are the dominant source of ion *number* flux onto Callisto's atmosphere, with the maximum flux more than a factor of 2 larger than those of oxygen and sulfur, since protons are the most abundant ion population in the ambient plasma below energies of  $E \approx 100$  keV, after which the differential fluxes between the three species are similar (see Figure 3). However, the largest contribution to the ion *energy* flux stems from sulfur, which dominates over the oxygen and proton

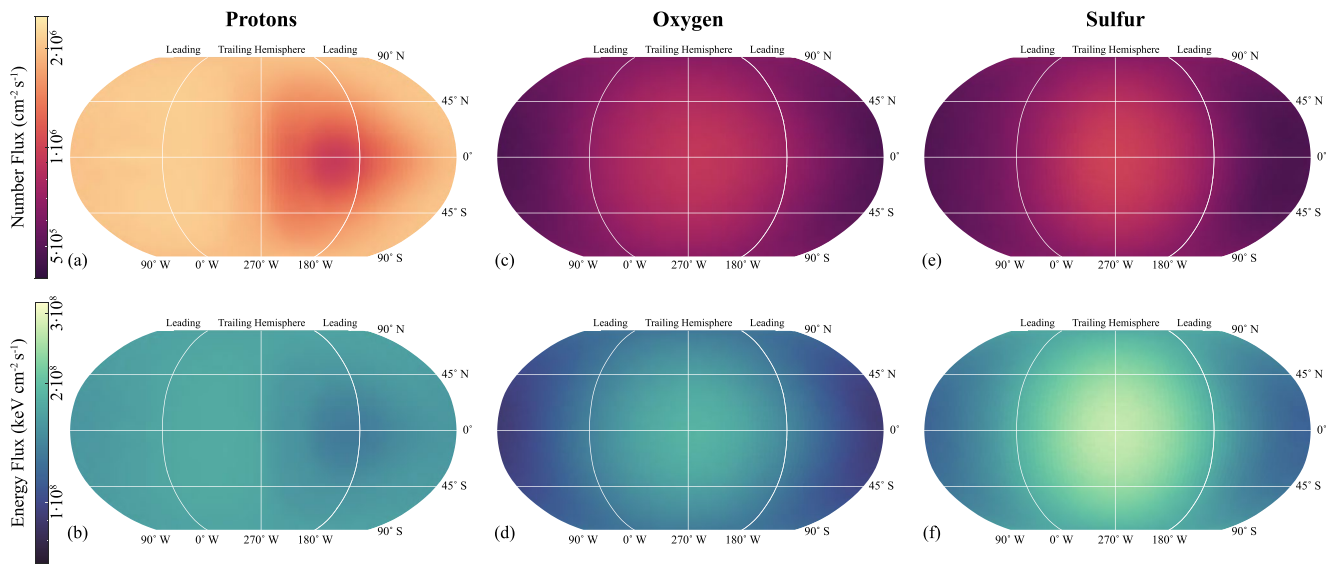


**Figure 6.** Energetic (a–b) proton (c–d) oxygen, and (e–f) sulfur (top row) number and (bottom row) energy fluxes onto the top of Callisto's atmosphere when located near the center of the Jovian current sheet. Note the narrower range of the color scales compared to Figure 4.

contributions by more than a factor of 3. Although protons are more abundant than oxygen or sulfur in the upstream plasma at the low-end of the energy range used in this study (see Figure 3), there are more sulfur ions at higher energies than the other two species. Hence, since sulfur ions dominate the most energetic population, they impart more energy into Callisto's exobase than the lighter ions.

Figure 6 also more clearly illustrates a broad-scale longitudinal non-uniformity in the ion flux within Callisto's anti-Jovian hemisphere that is predominantly caused by an asymmetry in the proton flux pattern. Near 90°W longitude, the proton number flux onto the top of Callisto's atmosphere exceeds that near 180°W by a factor of 2. This disparity is correlated with the location of the magnetic field pileup region, which is shifted into Callisto's anti-Jovian hemisphere (see Figure 2e) and is caused by two competing effects.

The first effect that contributes to the flux depletion in the sub-Jovian hemisphere is the gradient drift velocity acting on the ions when embedded within the pileup region. For a magnetic field that is mainly oriented southward (see Table 1 and Figure 1) and a magnetic field gradient within the pileup region mainly along the  $+\hat{x}$  direction, the gradient drift velocity points along the  $-\hat{y}$  direction (i.e., in the direction away from Jupiter). Hence, ions that approach Callisto from upstream that enter this region are deflected into the  $y < 0$  hemisphere (i.e., protons in the anti-Jovian hemisphere are directed away from the moon), thereby contributing to a reduced proton flux in the anti-Jovian exobase near longitudes of 180°W.

The second effect causing this reduction is a change to the gyroradii of the ions. A 4.5 keV proton in the ambient magnetic field near Callisto when embedded within the Jovian magnetospheric current sheet has a gyroradius of  $r_g \sim 1R_C$ . Hence, even for the lowest energies considered in this study, a proton in unperturbed fields would be able to gyrate around Callisto without impacting the moon. However, within the magnetic pileup region, the field strength increases by a factor of 5 and extends broadly in Callisto's anti-Jovian,  $y < 0$  hemisphere (see Figures 1e and 2e). As a result, proton gyroradii decrease within this region, and the energy at which a proton's gyrocircle is larger than Callisto increases by a factor of 5<sup>2</sup>, exceeding 100 keV. Hence, protons approaching Callisto from upstream that enter the pileup region are no longer able to gyrate around the moon to access any position of its exobase. The reduced gyroradii within this region of enhanced magnetic field, in combination with the direction of the gradient drift velocity pulling the protons *away* from this region, increases the likelihood that protons are able to travel past the moon without impacting the anti-Jovian exobase.

In comparison, protons that approach the moon in the sub-Jovian hemisphere are exposed to a *reduced* field strength (see Figure 2e). Their gyroradii therefore always exceed  $1R_C$ , implying a greater likelihood of precipitation onto the sub-Jovian exobase. In addition, the direction of the gradient drift in this hemisphere is directed *toward* Callisto for a proton located in the sub-Jovian hemisphere, thereby facilitating enhanced fluxes in this

region compared to the anti-Jovian hemisphere. Hence, these two effects result in the longitudinal asymmetry in the proton flux pattern visible in panel 6a. The heavy ion species are less affected by the change in magnetic field strength, since their gyroradii are nearly always at least as large as Callisto, even within the enhanced fields of the pileup region. Hence, only a weak leading/trailing asymmetry is visible in the oxygen and sulfur flux patterns centered around the trailing apex, consistent with the direction of the magnetospheric drift.

#### 4.2. Callisto Far Outside of the Jovian Current Sheet

Figure 7 displays the energetic particle flux onto the top of Callisto's atmosphere when the moon is located (7a–7d) far above and (7e–7h) far below the center of the Jovian current sheet. Compared to the electron influx patterns near the center of the sheet, the flux patterns with Callisto located far above and below the sheet display less fine structure. The most striking feature in the fluxes is a narrow band of low flux that separates two regions of enhanced flux and wraps globally around Callisto, clearly visible in the energetic electron patterns. For the case of Callisto located far above the Jovian current sheet center (panels 7a–7d), this band reaches latitudes of  $\sim 45^\circ\text{S}$  within the sub-Jovian hemisphere, passes through the equator near the leading and trailing apices, and extends to  $\sim 45^\circ\text{N}$  latitude in the anti-Jovian hemisphere. Within this band, electron fluxes are reduced by more than an order of magnitude compared to their maximum values. High-flux regions occur near  $0^\circ\text{W}$  and  $180^\circ\text{W}$  longitude, in the hemisphere opposite the band of reduced flux (e.g., with Callisto above the current sheet, the maximum flux in the sub-Jovian hemisphere occurs near  $45^\circ\text{N}$ , while the minimum flux is near  $45^\circ\text{S}$ ).

The band of reduced flux is coincident with the locations where the magnetic field is tangential to Callisto's exobase. The tilt of the magnetospheric background field in the  $\pm\hat{y}$  direction causes this band to appear “wavy” when projected onto the exobase (for a case with no plasma interaction currents and  $\mathbf{B}_0$  entirely along the  $\pm\hat{z}$  direction, this band would exactly coincide with the moon's equator; see, e.g., Breer et al., 2019). Conversely, high-flux regions correspond to those locations where the magnetic field is nearly radial to the moon (see also Liuzzo et al., 2019a, 2019b).

Electrons with small gyroradii ( $r_g \ll R_C$  for energies below  $\sim 0.5$  MeV; see Table 2) mainly approach Callisto along the magnetospheric field lines. As they encounter the moon, these particles are channeled toward regions where the magnetic field is mainly radial (and, due to the superposition of the magnetospheric background and induced field, where the magnitude is reduced; see Figure 1), thereby resulting in an enhanced particle flux at these locations. When Callisto is located above the center of the sheet, the projection of the background field onto Callisto would point from the top left to the bottom right in panels 7a–7d. Hence, for this case, the regions of maximum flux (where the field is mainly radial to the exobase) are centered near  $45^\circ\text{N}$  latitude in the sub-Jovian hemisphere, and  $45^\circ\text{S}$  latitude in the anti-Jovian hemisphere. The band of reduced electron fluxes therefore represents the region on Callisto where higher-energy electrons with less field-aligned velocities are able to gyrate beyond these regions to access locations where the magnetic field becomes more tangential to the exobase. However, since with increasing energy more particles are able to gyrate around Callisto, they are able to deposit their flux onto more global locations and this band of reduced flux disappears with the flux patterns approaching homogeneity.

With Callisto located far below the sheet (panels 7e–7h), the electron flux patterns are mirrored across the equator, with the band of reduced flux extending into the northern hemisphere on the sub-Jovian side of the moon and into the southern hemisphere on the anti-Jovian side. This is caused by the difference in the orientation of the background magnetospheric field, which mainly points away from Jupiter above the current sheet center, but toward Jupiter below the sheet (see Table 1). Indeed when located below the sheet, the projection of the field onto Callisto is (nearly) mirrored across the  $270^\circ\text{W}$  longitude line, pointing from the top right toward the lower left in panels 7e–7h.

For this case near  $0^\circ\text{W}$  and  $180^\circ\text{W}$  longitudes, a region of slightly reduced electron fluxes is “carved out” of the more broad-scale flux maxima, causing rings in the electron fluxes that encircle the sub- and anti-Jovian hemisphere apices. This is most clearly visible in the electron energy flux pattern with Callisto located far below the current sheet center (panels 7e–7f). Within these regions, the presence of Callisto's induced dipole causes the local field to be more tangential to the moon, reducing the accessibility of this region to the energetic particles and thereby resulting in a (comparatively) reduced flux (see also Figure 11 presented in Liuzzo et al., 2019b).

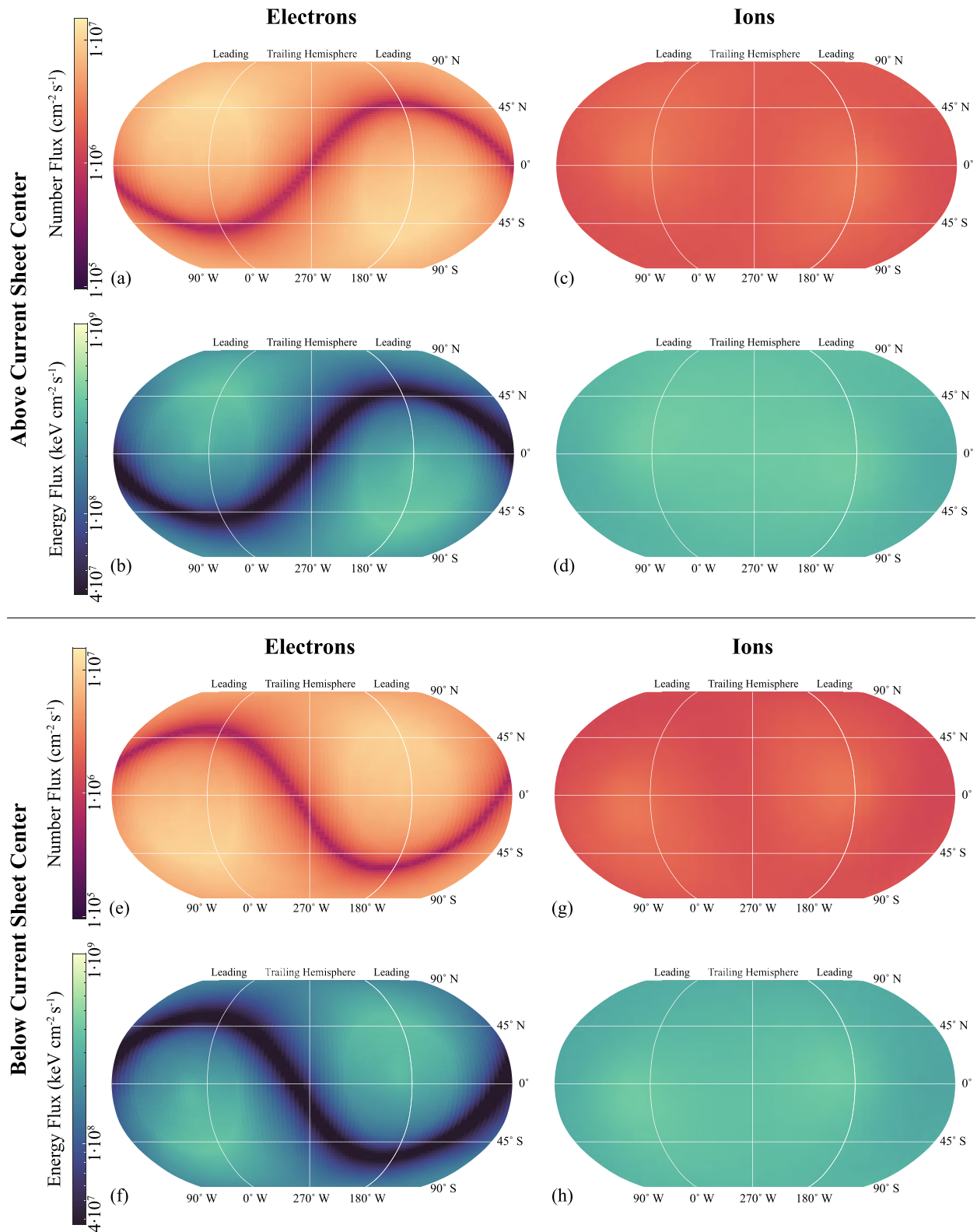


**Figure 7.** Energetic electron and ion fluxes onto the top of Callisto's atmosphere in the same style as Figure 4, but for times when the moon is located (a–d) above and (e–h) below the center of the Jovian current sheet. The color scales are identical to the ones used in Figure 4.

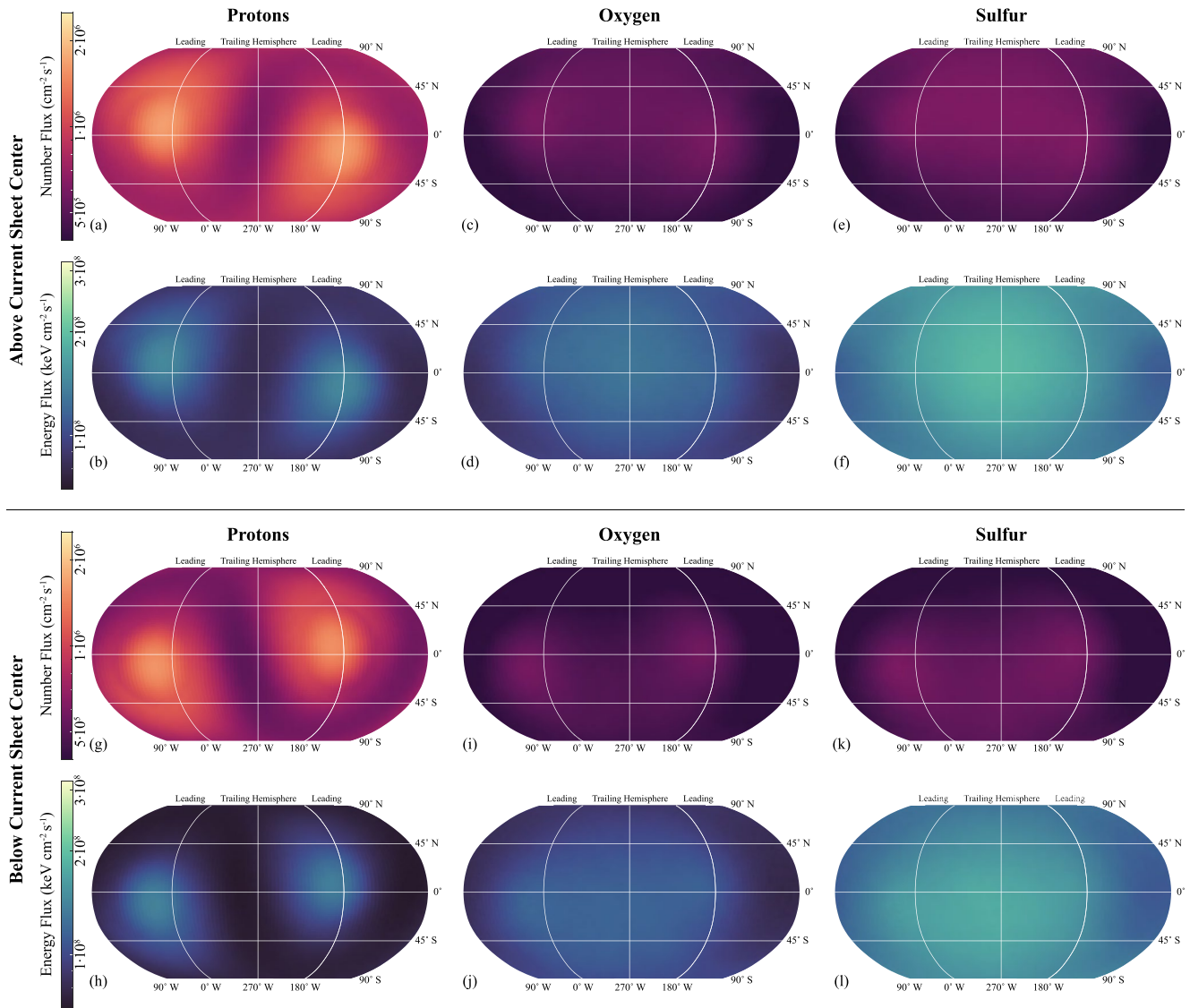


**Figure 8.** Energetic ion fluxes in the same style as Figure 6, but for times when Callisto is located at maximum distances (a–f) above and (g–l) below the center of the Jovian current sheet. Color scales are identical compared to Figure 6, but are more narrow compared to Figure 7.

For ions, the gyroradius of a 4.5 keV proton (i.e., the lowest energy considered for this study) when far from the center of the current sheet is already  $\sim 10\%$  of a Callisto radius (see Table 2). Hence even at these energies, gyration plays a non-negligible role in shaping the flux patterns onto the exobase, and this process is only subtly visible in the ion fluxes presented in Figure 7. To more clearly illustrate the slight inhomogeneity in the ion flux patterns, and for a more straightforward comparison to the ion fluxes onto Callisto when located within the Jovian current sheet, contributions from the individual ion species to the total ion flux are included in Figure 8. This figure illustrates a similar tendency in the energetic ion fluxes as was visible for the electrons in Figure 7 with a band of reduced ion fluxes located wherever the magnetic field is mainly tangential to the exobase.

Even still, the global fluxes are nearly homogeneous for the energetic ions: differences between the minima and maxima are far less extreme than the differences present in the flux patterns of the electrons. A similar band of reduced energetic ion flux has been suggested to form at Jupiter's moon Europa, as well (see Addison et al., 2021; Breer et al., 2019). The band of reduced flux splitting the two regions of higher flux is most clearly evident for protons, which have the lowest gyroradii at a given energy compared to oxygen or sulfur. For the heavy ions on the other hand, the patterns are much more homogeneous, since their gyroradii already approach the size of Callisto at much lower energies and are able to gyrate onto nearly any point of the moon (see Table 2). As with

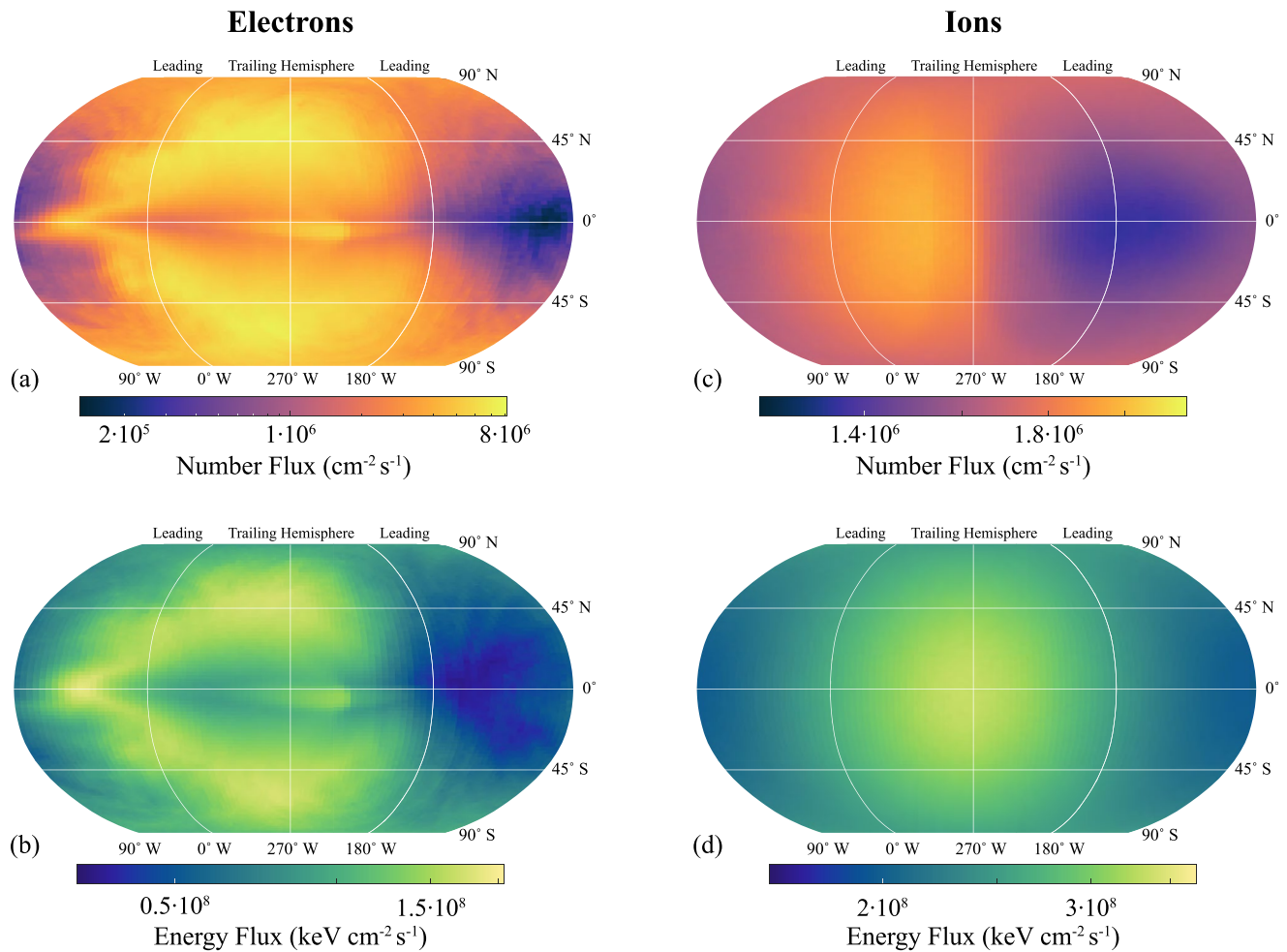


**Figure 9.** Averaged energetic (a–b) electron and (c–d) ion fluxes deposited onto Callisto's exobase over a full synodic period. Note that different color scales are used between each panel in order to enhance visibility of the flux features.

Callisto embedded within the current sheet, the protons' contribution to the total ion number flux exceeds those of oxygen and sulfur, whereas the energy flux is again dominated by the sulfur ions. Finally, as also seen for electrons, the ion fluxes are nearly mirrored across the equator when comparing the patterns onto the exobase when Callisto is located above and below the current sheet.

## 5. Discussion

To estimate the energetic ion and electron fluxes deposited onto Callisto's exobase over the course of a synodic period, Figure 9 presents averaged maps of the energetic particle flux. Such an understanding of this averaged case is powerful, since modification of Callisto's icy surface happens over geologic timescales: any asymmetries in the particle fluxes onto the moon's exobase averaged over a synodic period may portend disparities in the bombardment and weathering of Callisto's surface. To obtain these maps, we average the incident fluxes onto Callisto's exobase from Section 4 with the moon located within, above, and below the magnetospheric current sheet that were presented in Figures 4 and 7. Since Callisto passes through the center of the sheet twice during a synodic period, the fluxes for the case of the moon located within the sheet are included twice for the average. In addition, to represent the reduction in the abundance of energetic particles when Callisto is located far above and below the current sheet, the fluxes onto the exobase for these two cases are reduced by a factor of 10 compared to those presented in Figure 7.



We note that reducing the fluxes onto Callisto's exobase by an order of magnitude when far outside of the current sheet is only an approximation. Limited measurements exist that constrain how the differential flux of the energetic particles outside of Callisto's interaction region is affected by System III longitude (i.e., Callisto's distance to the center of the current sheet). Paranicas et al. (2018) have shown that during a synodic period, the magnetic distance of field lines to which the moon is connected ranges from  $26.3R_J$  (when located within the Jovian magnetospheric current sheet) to beyond  $70R_J$  (when located far outside of the sheet; see also Figure 2 of Liuzzo et al., 2019a). As illustrated in Figure 3, the differential flux of the ambient magnetospheric energetic particle population measured by the Juno spacecraft drops by over an order of magnitude between these cases, which is also consistent with Galileo observations (Kollmann et al., 2018). However, the differential energetic particle fluxes when Callisto is located far outside the sheet are not reduced by a factor of exactly 10 compared to those within the sheet at every energy, so the total integrated influx onto the top of the exobase may be slightly different for these two cases in reality. Regardless, applying this approximation allows us to estimate how changes in the energetic particle abundances to which Callisto is exposed at various System III longitudes affect the fluxes onto the moon's exosphere over a full synodic period.

As illustrated in Figure 9, the synodically averaged fluxes are nearly indistinguishable from those when the moon is located within the current sheet (cf. Figure 4). Averaged over Callisto's entire exobase, the number and energy fluxes in Figure 9 are within a factor of 1.9 of the globally averaged value with Callisto located within the current sheet. As in Figure 4, a global leading/trailing asymmetry in the electron fluxes is still visible and the effect of local perturbations to the magnetic field again imprints into the patterns. For example, the wedge of enhanced flux in Callisto's sub-Jovian, leading hemisphere is present where electrons are channeled into the thin sheet of reduced magnetic field within the moon's wake (see also Figure 5). For ions and electrons, the magnetic field pileup region reduces the number fluxes in the moon's anti-Jovian hemisphere—an effect that is not present when Callisto is located at maximum distances from the center of the sheet (cf. Figures 7 and 8). These similarities of the synodically averaged fluxes to the fluxes within the current sheet are predominantly driven by the vastly enhanced energetic particle abundance with Callisto located near the center of the current sheet compared to far outside of it. Figure 9 therefore highlights that the fluxes deposited onto Callisto's exobase when the moon is located near the center of the current sheet are representative of the averaged fluxes over a synodic rotation—assuming an order of magnitude difference in the energetic particle abundances (which is consistent with observations; see Figure 3). Therefore, the perturbed electromagnetic environment generated by Callisto's interaction with the ambient thermal magnetospheric plasma when near the center of the magnetospheric current sheet plays a stronger role in shaping the fluxes of  $4.5 \text{ keV} \leq E \leq 11.8 \text{ MeV}$  particles onto the exobase than does the plasma interaction when far from the sheet or the presence of the moon's induced field. An accurate representation of these perturbed fields is therefore critical when constraining the average energetic particle fluxes onto the exobase over a synodic period.

To further illustrate the differences between the fluxes onto Callisto's atmosphere when located above, within, and below the Jovian current sheet, Table 3 provides averaged fluxes for these three scenarios. As in Figure 9, the values in Table 3 for the “Above Sheet” and “Below Sheet” cases have been reduced by a factor of 10 compared to the values presented in Section 4.2. As expected, Table 3 illustrates that the electron and ion fluxes onto Callisto's exobase when located within the current sheet therefore exceed those onto the moon when located far outside of the sheet by at least an order of magnitude. However, for all positions of Callisto with respect to the Jovian current sheet, the averaged number flux of energetic electrons onto the top of the moon's atmosphere exceeds the sum of the averaged ion number fluxes (as is the case in the ambient, undisturbed plasma; see Figure 3). Far outside of the current sheet, the electron number flux is three times larger than the ion fluxes, while within the sheet, the flux is nearly twice as large. As also visible in Figures 4 and 7, the average energy flux is dominated by the energetic ion contribution for all three cases. The largest difference (a factor of  $\sim 5$ ) occurs near the center of the current sheet, with an electron to ion ratio of 0.21.

In addition to the global averages of the number and energy fluxes, Table 3 breaks down the ion and electron number fluxes onto Callisto's atmosphere into four separate hemispheres: leading (longitudes between  $0^\circ\text{W}$  and  $180^\circ\text{W}$ ), trailing (between  $180^\circ\text{W}$  and  $360^\circ\text{W}$ ), northern (latitudes from  $0^\circ\text{N}$  to  $90^\circ\text{N}$ ), and southern (between  $0^\circ\text{S}$  and  $90^\circ\text{S}$ ). When located far outside of the Jovian current sheet, the ion and electron number fluxes onto the moon's trailing hemisphere are approximately equal to those deposited onto the leading hemisphere (to within  $\sim 5\%$ ). Hence, there is no strong global asymmetry to the irradiation of Callisto's exobase for these cases far outside of the current sheet. Similarly within the center of the sheet, the ion fluxes onto the leading and trailing

**Table 3**

*Total Energetic Particle Precipitation Rates and Averaged Fluxes Onto the Top of Callisto's Atmosphere When Located Above, Within, and Below the Jovian Current Sheet<sup>a</sup>*

|                                        | Electrons | Ions | Ratio | Hydrogen | Oxygen | Sulfur |
|----------------------------------------|-----------|------|-------|----------|--------|--------|
| <b>Above sheet<sup>b</sup></b>         |           |      |       |          |        |        |
| Precipitation rate ( $\cdot 10^{28}$ ) | 0.41      | 0.14 | 2.9   | 0.06     | 0.03   | 0.04   |
| Global number flux ( $\cdot 10^6$ )    | 0.57      | 0.19 | 3.0   | 0.09     | 0.05   | 0.05   |
| Global energy flux ( $\cdot 10^8$ )    | 0.17      | 0.36 | 0.47  | 0.10     | 0.11   | 0.15   |
| Leading number flux ( $\cdot 10^6$ )   | 0.57      | 0.19 | 3.0   | 0.09     | 0.05   | 0.05   |
| Trailing number flux ( $\cdot 10^6$ )  | 0.56      | 0.20 | 2.8   | 0.09     | 0.05   | 0.06   |
| Northern number flux ( $\cdot 10^6$ )  | 0.57      | 0.20 | 2.9   | 0.09     | 0.05   | 0.06   |
| Southern number flux ( $\cdot 10^6$ )  | 0.56      | 0.18 | 3.1   | 0.09     | 0.05   | 0.05   |
| <b>Within sheet</b>                    |           |      |       |          |        |        |
| Precipitation rate ( $\cdot 10^{28}$ ) | 5.3       | 2.3  | 2.3   | 1.3      | 0.48   | 0.48   |
| Global number flux ( $\cdot 10^6$ )    | 7.3       | 3.2  | 2.3   | 1.8      | 0.67   | 0.66   |
| Global energy flux ( $\cdot 10^8$ )    | 2.2       | 4.8  | 0.21  | 1.6      | 1.3    | 1.8    |
| Leading number flux ( $\cdot 10^6$ )   | 5.0       | 3.1  | 2.3   | 1.9      | 0.58   | 0.56   |
| Trailing number flux ( $\cdot 10^6$ )  | 9.7       | 3.3  | 2.9   | 1.8      | 0.75   | 0.76   |
| Northern number flux ( $\cdot 10^6$ )  | 7.0       | 3.2  | 2.2   | 1.9      | 0.67   | 0.66   |
| Southern number flux ( $\cdot 10^6$ )  | 7.7       | 3.2  | 2.4   | 1.8      | 0.67   | 0.66   |
| <b>Below sheet<sup>b</sup></b>         |           |      |       |          |        |        |
| Precipitation rate ( $\cdot 10^{28}$ ) | 0.36      | 0.12 | 3.0   | 0.06     | 0.03   | 0.03   |
| Global number flux ( $\cdot 10^6$ )    | 0.50      | 0.17 | 2.9   | 0.08     | 0.04   | 0.05   |
| Global energy flux ( $\cdot 10^8$ )    | 0.15      | 0.33 | 0.45  | 0.08     | 0.10   | 0.14   |
| Leading number flux ( $\cdot 10^6$ )   | 0.51      | 0.16 | 3.2   | 0.08     | 0.04   | 0.04   |
| Trailing number flux ( $\cdot 10^6$ )  | 0.50      | 0.17 | 2.9   | 0.08     | 0.05   | 0.05   |
| Northern number flux ( $\cdot 10^6$ )  | 0.50      | 0.16 | 3.1   | 0.08     | 0.04   | 0.04   |
| Southern number flux ( $\cdot 10^6$ )  | 0.51      | 0.18 | 2.8   | 0.08     | 0.05   | 0.05   |

<sup>a</sup>Fluxes of individual ion species are provided in addition to the sum. The electron-to-ion flux ratio is also included. Precipitation rates (i.e., the total number of particles precipitating globally onto the exobase per second) are provided in units of  $s^{-1}$ , number fluxes are given in units of  $cm^{-2} s^{-1}$ , and units of energy fluxes are in  $keV cm^{-2} s^{-1}$ . <sup>b</sup>When Callisto is located far above or below the current sheet, the abundance of energetic particles in the ambient plasma is reduced by at least an order of magnitude compared to when Callisto is located within the sheet (see Figure 3). To represent this, the values in this table for these two cases have been reduced by an order of magnitude compared to the discussion in Section 4.2. See text for further details.

hemispheres are approximately equal with the largest asymmetry for the ions in this case is between the sub- and anti-Jovian hemispheres (see Figure 6). However, the largest asymmetry occurs in the electron number flux onto Callisto's trailing exobase, which is nearly two times larger than the flux onto the leading hemisphere with the moon embedded within the Jovian current sheet. This is consistent with the substantial leading/trailing asymmetry visible in the electron flux pattern displayed in Figure 4a and may therefore suggest a strong longitudinal asymmetry to the energy deposition into Callisto's atmosphere (and potentially its surface) by energetic electrons.

Compared to a hypothetical case where all of the energetic particles in Callisto's ambient magnetospheric environment uniformly reach the moon, the moon's plasma interaction reduces the electron and ion number fluxes onto the exobase. For electrons, the flux is reduced by over an order of magnitude ( $3.8 \cdot 10^8 cm^{-2} s^{-1}$  compared to  $7.3 \cdot 10^6 cm^{-2} s^{-1}$ ), while for ions, the flux is lower by a factor of  $\sim 5$  (see Section 4.1). However, in comparison to the other two cases with the moon located far outside of the Jovian magnetospheric current sheet, Table 3 illustrates that, because of the vastly enhanced abundance of energetic particles within the ambient magnetospheric plasma when Callisto is near the current sheet center (see also Figure 3), Callisto's interaction is unable to effectively shield the exobase from precipitation of energetic particles. Rather, the total energetic particle fluxes averaged across each point of the exobase is enhanced within the sheet compared to the other two cases far outside

of it. Within the current sheet, the globally averaged ion fluxes, as well as the total number of ions bombarding the exobase per second, are nearly 20 times larger compared to when the moon is outside of the sheet. For electrons, these values within the sheet are more than 10 times larger than when located outside of it. As such, the flux patterns onto Callisto's exobase when located near the center of the Jovian current sheet contribute most strongly to the flux onto the moon averaged over a synodic period.

The energetic ion and electron fluxes onto the top of Callisto's atmosphere can also be compared to the fluxes onto other solar system moons. Similar to within the polar regions of Jupiter's moon Ganymede (i.e., poleward of the open-closed field line boundary), the electron fluxes onto Callisto exceed the sum of the ion fluxes. However, the difference between the two populations is even more extreme at Ganymede, where energetic electron surface fluxes are up to an order of magnitude larger than the contribution from ions (e.g., Liuzzo et al., 2020). Longitudinal asymmetries that are present in the energetic ion and electron flux patterns onto equatorial latitudes of Ganymede are mainly associated with these particles' senses of gradient and curvature drifts within the closed field line region of the moon's mini-magnetosphere (e.g., Liuzzo et al., 2020; Poppe et al., 2018; Williams et al., 1997). At Europa, the fluxes of energetic ions onto the surface are similarly quasi-uniform. Slight longitudinal asymmetries in the ion patterns onto Europa's surface in which the flux deposited onto the trailing hemisphere is reduced below the leading hemisphere flux (Addison et al., 2021), and a belt of reduced fluxes forms wherever the magnetic field is tangential to the surface (Breer et al., 2019), as also seen here at Callisto. However, the degree to which the flux patterns of electrons precipitating onto Europa are affected by the perturbed electromagnetic environment remains unknown. Finally, at Saturn's moon Titan, precipitation of ions at energies  $E < 10$  keV has been shown to be a key role in understanding the ionization of, and energy deposition into, this moon's dense atmosphere, with ionization rates from ions being comparable to those from electrons (e.g., Snowden & Higgins, 2021; Snowden et al., 2018). Particles at these energies may therefore also contribute to ionization of Callisto's atmosphere in an important way.

## 6. Conclusions

This study has investigated the effect of Callisto's perturbed electromagnetic environment on the energetic ion and electron fluxes deposited onto the top of the atmosphere. We have constrained signatures associated with the interaction of Callisto's induced dipole and ionosphere with the low-energy magnetospheric plasma—generating magnetospheric field line pileup, draping, and mass loading signatures—which change with the moon's distance to the center of the Jovian magnetospheric current sheet. For three representative scenarios of this thermal plasma interaction over a synodic period, we have quantified the effect of the variability in the electromagnetic draping pattern on the energetic magnetospheric electron, proton, oxygen, and sulfur fluxes that are deposited onto the top of Callisto's atmosphere. Our key results can be summarized as follows:

1. Callisto's interaction with the Jovian magnetospheric plasma most strongly perturbs the electromagnetic environment when the moon is embedded within the Jovian current sheet. Within the upstream pileup region, the magnetic field is enhanced by a factor of 5 compared to its background value, while downstream of the moon, a depression forms where the field magnitude is reduced to less than half of its ambient strength. These signatures are highly asymmetric along the direction of the convective electric field, due to the large gyroradii of the ionospheric pickup species near the moon. At large distances above and below the sheet, the plasma interaction currents are weak: perturbations to Callisto's local magnetic environment are mainly generated by the moon's induced field.
2. Despite strong plasma interaction currents, the energetic particle fluxes onto Callisto's exobase are maximized when the moon is located near the center of the Jovian magnetospheric current sheet:
  - 2.1 For electrons, compared to a hypothetical case with no plasma currents, Callisto's plasma interaction reduces the flux onto the exobase by nearly two orders of magnitude. However, since the abundance of the ambient energetic populations decrease by at least an order of magnitude when the moon is located far outside of the current sheet, the electron flux deposited onto the exobase is maximized when Callisto is located near the current sheet center. As a result, the pattern of the electron flux onto Callisto's exobase averaged over a full synodic period resembles that when the moon is embedded within the current sheet. Under these conditions, electron fluxes are partitioned into a high-flux region in the moon's trailing hemisphere, and a low-flux region in the leading hemisphere. An additional east/west asymmetry to the fluxes is present as well. In Callisto's leading, sub-Jovian hemisphere, the magnetic depletion region formed by

the plasma interaction funnels electrons toward the moon, locally enhancing fluxes. In the anti-Jovian hemisphere, the magnetic field pileup region—dragged along the convective electron field direction by the motion of the low-energy ionospheric pickup ions—reduces the electron fluxes.

- 2.2 For ions, the plasma interaction currents only reduce the fluxes by a factor of  $\sim 5$  when compared to the uniform, undisturbed case, since the patterns of the ion fluxes onto the top of Callisto's atmosphere are only weakly affected by the moon's plasma interaction. Instead, the large gyroradii of energetic ions in the magnetic field near the moon result in a nearly homogeneous map of the fluxes for all positions with respect to the Jovian magnetospheric current sheet. Similar to electrons, the ion fluxes onto the exobase with Callisto located near the Jovian current sheet center dominate those fluxes when the moon is far from the current sheet, due to the drop in the abundance of the energetic ion population with increasing distance to the sheet.
3. The contribution of electrons to the averaged number flux is approximately 3 times larger than the contributions from the ions for all three scenarios presented in this study. Conversely, energetic ions are responsible for the majority of the energy flux deposited onto the atmosphere, exceeding the electron energy flux by up to a factor of 3.
4. Due to the order of magnitude difference in the energetic particle abundance near Callisto within the magnetospheric current sheet compared to far outside of it, the fluxes and precipitation patterns of energetic particles onto Callisto's exobase when the moon is located near the center of the sheet provide a good approximation for the fluxes averaged over a full synodic period.

This study has highlighted the fundamental importance of accurately representing Callisto's interaction with its ambient magnetospheric environment when investigating energetic particle fluxes onto the moon, and has constrained the effect that these perturbed fields have on the particle fluxes deposited onto the moon's exobase. However, since Callisto's atmosphere is dense and potentially collisional (e.g., Carberry Mogan et al., 2021; Cunningham et al., 2015), the energetic particle fluxes onto the top of the atmosphere may *not* equal the flux that reaches the surface. Therefore, a rigorous investigation of the effects that the atmosphere has on the energetic particles should be undertaken before attempting to correlate precipitation patterns with surface features or applying the fluxes to obtain, for example, surface sputtering rates or energy irradiation at depth. These atmosphere-particle effects—including the resulting energy loss of the particles as they precipitate before reaching the surface—are open questions at Callisto, and will be investigated in a future study.

## Data Availability Statement

All data products from this study can be obtained from <https://doi.org/10.5281/zenodo.6784734>. Data from the Juno mission presented in this study is available at the Planetary Data System (<https://pds-ppi.igpp.ucla.edu/search/?t=Jupiter&sc=Juno&facet=SPACECRAFTNAME&depth=1>).

## Acknowledgments

The authors acknowledge support from NASA Solar System Workings Grant 80NSSC21K0152 and 80NSSC22K0097, and NASA New Frontiers Data Analysis Program Grant 80NSSC21K0823.

This research used the Savio computational cluster resource provided by the Berkeley Research Computing program at the University of California, Berkeley (supported by the UC Berkeley Chancellor, Vice Chancellor for Research, and Chief Information Officer). This research was also supported in part through research cyberinfrastructure resources and services provided by the Partnership for an Advanced Computing Environment at the Georgia Institute of Technology, Atlanta, Georgia, USA.

## References

- Addison, P., Liuzzo, L., Arnold, H., & Simon, S. (2021). Influence of Europa's time-varying electromagnetic environment on magnetospheric ion precipitation and surface weathering. *Journal of Geophysical Research: Space Physics*, 126(5), 1–42. <https://doi.org/10.1029/2020ja029087>
- Addison, P., Liuzzo, L., & Simon, S. (2022). Effect of the magnetospheric plasma interaction and solar illumination on ion sputtering of Europa's surface ice. *Journal of Geophysical Research: Space Physics*, 127(2), 1–39. <https://doi.org/10.1029/2021JA030136>
- Bagenal, F., & Delamere, P. A. (2011). Flow of mass and energy in the magnetospheres of Jupiter and Saturn. *Journal of Geophysical Research*, 116(A5), A05209. <https://doi.org/10.1029/2010JA016294>
- Bagenal, F., Wilson, R. J., Siler, S., Paterson, W. R., & Kurth, W. S. (2016). Survey of Galileo plasma observations in Jupiter's plasma sheet. *Journal of Geophysical Research: Planets*, 121(5), 871–894. <https://doi.org/10.1002/2016JE005009>
- Belcher, J. W. (1983). The low-energy plasma in the Jovian magnetosphere. *Physics of the Jovian magnetosphere*, 1, 68–105. <https://doi.org/10.1017/cbo9780511564574.005>
- Bhattacharyya, D., Clarke, J. T., Montgomery, J., Bonfond, B., Gérard, J.-C., & Grodent, D. (2017). Evidence for auroral emissions from Callisto's footprint in HST UV images. *Journal of Geophysical Research: Space Physics*, 123(1), 364–373. <https://doi.org/10.1002/2017JA024791>
- Boris, J. P. (1970). Relativistic plasma simulation-optimization of a hybrid code. In *Proceedings of the 4th conference on numerical simulation of plasmas* (pp. 3–67). Naval Research Laboratory.
- Breer, B. R., Liuzzo, L., Arnold, H., Andersson, P. N., & Simon, S. (2019). Energetic ion dynamics in the perturbed electromagnetic fields near Europa. *Journal of Geophysical Research: Space Physics*, 124(9), 7592–7613. <https://doi.org/10.1029/2019JA027147>
- Carberry Mogan, S. R., Tucker, O. J., Johnson, R. E., Sreenivasan, K. R., & Kumar, S. (2020). The influence of collisions and thermal escape in Callisto's atmosphere. *Icarus*, 352, 113932. <https://doi.org/10.1016/j.icarus.2020.113932>
- Carberry Mogan, S. R., Tucker, O. J., Johnson, R. E., Vorburger, A., Galli, A., Marchand, B., et al. (2021). A tenuous, collisional atmosphere on Callisto. *Icarus*, 368, 114597. <https://doi.org/10.1016/j.icarus.2021.114597>

- Carlson, R. W. (1999). A tenuous carbon dioxide atmosphere on Jupiter's moon Callisto. *Science*, 283(5403), 820–821. <https://doi.org/10.1126/science.283.5403.820>
- Clark, G., Mauk, B. H., Kollmann, P., Paranicas, C., Bagenal, F., Allen, R. C., et al. (2020). Heavy ion charge states in Jupiter's polar magnetosphere inferred from auroral Megavolt electric potentials. *Journal of Geophysical Research: Space Physics*, 125(9), 1–12. <https://doi.org/10.1029/2020JA028052>
- Clark, G., Mauk, B. H., Paranicas, C., Kollmann, P., & Smith, H. T. (2016). Charge states of energetic oxygen and sulfur ions in Jupiter's magnetosphere. *Journal of Geophysical Research: Space Physics*, 121(3), 2264–2273. <https://doi.org/10.1002/2015JA022257>
- Collier, M. R., & Hamilton, D. C. (1995). The relationship between kappa and temperature in energetic ion spectra at Jupiter. *Geophysical Research Letters*, 22(3), 303–306. <https://doi.org/10.1029/94GL02997>
- Connerney, J. E. P., Acuña, M. H., Ness, N. F., & Satoh, T. (1998). New models of Jupiter's magnetic field constrained by the Io flux tube footprint. *Journal of Geophysical Research*, 103(A6), 11929–11939. <https://doi.org/10.1029/97JA03726>
- Cooper, J. F., Johnson, R. E., Mauk, B. H., Garrett, H. B., & Gehrels, N. (2001). Energetic ion and electron irradiation of the icy Galilean satellites. *Icarus*, 149(1), 133–159. <https://doi.org/10.1006/icar.2000.6498>
- Cunningham, N. J., Spencer, J. R., Feldman, P. D., Strobel, D. F., France, K., & Osterman, S. N. (2015). Detection of Callisto's oxygen atmosphere with the Hubble space telescope. *Icarus*, 254, 178–189. <https://doi.org/10.1016/j.icarus.2015.03.021>
- Dalton, J. B., Cassidy, T., Paranicas, C., Shirley, J. H., Prockter, L. M., & Kamp, L. W. (2013). Exogenic controls on sulfuric acid hydrate production at the surface of Europa. *Planetary and Space Science*, 77, 45–63. <https://doi.org/10.1016/j.pss.2012.05.013>
- de Soria-Santacruz, M., Garrett, H. B., Evans, R. W., Jun, I., Kim, W., Paranicas, C., & Drozdov, A. (2016). An empirical model of the high-energy electron environment at Jupiter. *Journal of Geophysical Research A: Space Physics*, 121(10), 9732–9743. <https://doi.org/10.1002/2016JA023059>
- Fatemi, S., Poppe, A. R., Khurana, K. K., Holmström, M., & Delory, G. T. (2016). On the formation of Ganymede's surface brightness asymmetries: Kinetic simulations of Ganymede's magnetosphere. *Geophysical Research Letters*, 43(10), 4745–4754. <https://doi.org/10.1002/2016GL068363>
- Friedman, Y., & Semon, M. D. (2005). Relativistic acceleration of charged particles in uniform and mutually perpendicular electric and magnetic fields as viewed in the laboratory frame. *Physical Review E—Statistical, Nonlinear and Soft Matter Physics*, 72(2), 1–10. <https://doi.org/10.1103/PhysRevE.72.026603>
- Garrett, H. B., Jun, I., Ratliff, J. M., Evans, R. W., Clough, G. A., & McEntire, R. W. (2003). *Galileo Interim Radiation electron (GIRE) model*. JPL Publication, 03–006.
- Hartkorn, O., & Saur, J. (2017). Induction signals from Callisto's ionosphere and their implications on a possible subsurface ocean. *Journal of Geophysical Research: Space Physics*, 122(11), 677–711. <https://doi.org/10.1002/2017JA024269>
- Hartkorn, O., Saur, J., & Strobel, D. F. (2017). Structure and density of Callisto's atmosphere from a fluid-kinetic model of its ionosphere: Comparison with Hubble Space Telescope and Galileo observations. *Icarus*, 282, 237–259. <https://doi.org/10.1016/j.icarus.2016.09.020>
- Jun, I., Garrett, H. B., Cassidy, T. A., Kim, W., & Dougherty, L. (2019). Updating the Jovian electron plasma environment. *IEEE Transactions on Plasma Science*, 47(8), 3915–3922. <https://doi.org/10.1109/TPS.2019.2901681>
- Kabanovic, S., Feyerabend, M., Simon, S., Meeks, Z., & Wulms, V. (2018). Influence of asymmetries in the magnetic draping pattern at Titan on the emission of energetic neutral atoms. *Planetary and Space Science*, 152, 142–164. <https://doi.org/10.1016/j.pss.2017.12.017>
- Keppler, E., & Krupp, N. (1996). The charge state of helium in the Jovian magnetosphere: A possible method to determine it. *Planetary and Space Science*, 44(2), 71–75. [https://doi.org/10.1016/0032-0633\(95\)00076-3](https://doi.org/10.1016/0032-0633(95)00076-3)
- Khurana, K. K. (1992). A generalized hinged-magnetodisc model of Jupiter's nightside current sheet. *Journal of Geophysical Research*, 97(A5), 6269. <https://doi.org/10.1029/92ja00169>
- Khurana, K. K. (1997). Euler potential models of Jupiter's magnetospheric field. *Journal of Geophysical Research*, 102(A6), 11295–11306. <https://doi.org/10.1029/97JA00563>
- Khurana, K. K., Kivelson, M. G., Stevenson, D. J., Schubert, G., Russell, C. T., Walker, R. J., & Polansky, C. (1998). Induced magnetic fields as evidence for subsurface oceans in Europa and Callisto. *Nature*, 395(6704), 777–780. <https://doi.org/10.1038/27394>
- Khurana, K. K., Russell, C. T., & Dougherty, M. K. (2008). Magnetic portraits of Tethys and Rhea. *Icarus*, 193(2), 465–474. <https://doi.org/10.1016/j.icarus.2007.08.005>
- Kivelson, M., Bagenal, F., Kurth, W., Neubauer, F., Paranicas, C., & Saur, J. (2004). Magnetospheric interactions with satellites. In *Jupiter: The planet, satellites and magnetosphere* (pp. 513–536).
- Kivelson, M., Khurana, K., Stevenson, D., Bennett, L., Joy, S., Russell, C., et al. (1999). Europa and Callisto: Induced or intrinsic fields in a periodically varying plasma environment. *Journal of Geophysical Research*, 104(A3), 4609–4625. <https://doi.org/10.1029/1998JA900095>
- Kliore, A. J. J., Anabtawi, a., Herrera, R. G. G., Asmar, S. W. W., Nagy, A. F. F., Hinson, D. P. P., & Flasar, F. M. M. (2002). Ionosphere of Callisto from Galileo radio occultation observations. *Journal of Geophysical Research*, 107(A11), 1–7. <https://doi.org/10.1029/2002JA009365>
- Kollmann, P., Roussos, E., Paranicas, C., Woodfield, E. E., Mauk, B. H., Clark, G., et al. (2018). Electron acceleration to MeV energies at Jupiter and Saturn. *Journal of Geophysical Research: Space Physics*, 123(11), 9110–9129. <https://doi.org/10.1029/2018JA025665>
- Kotova, A., Roussos, E., Krupp, N., & Dandouras, I. (2015). Modeling of the energetic ion observations in the vicinity of Rhea and Dione. *Icarus*, 258, 402–417. <https://doi.org/10.1016/j.icarus.2015.06.031>
- Krupp, N., Roussos, E., Krieger, H., Kollmann, P., Kivelson, M. G. G., Kotova, A., et al. (2013). Energetic particle measurements in the vicinity of Dione during the three Cassini encounters 2005–2011. *Icarus*, 226(1), 617–628. <https://doi.org/10.1016/j.icarus.2013.06.007>
- Lindkvist, J., Holmström, M., Khurana, K. K., Fatemi, S., & Barabash, S. (2015). Callisto plasma interactions: Hybrid modeling including induction by a subsurface ocean. *Journal of Geophysical Research: Space Physics*, 120(6), 4877–4889. <https://doi.org/10.1002/2015JA021212>
- Liuzzo, L., Feyerabend, M., Simon, S., & Motschmann, U. (2015). The impact of Callisto's atmosphere on its plasma interaction with the Jovian magnetosphere. *Journal of Geophysical Research A: Space Physics*, 120(11), 9401–9427. <https://doi.org/10.1002/2015JA021792>
- Liuzzo, L., Paty, C., Cochrane, C., Nordheim, T., Luspay-Kuti, A., Castillo-Rogez, J., et al. (2021). Triton's variable interaction with Neptune's magnetospheric plasma. *Journal of Geophysical Research: Space Physics*, 126(11), 1–27. <https://doi.org/10.1029/2021ja029740>
- Liuzzo, L., Poppe, A. R., Paranicas, C., Nénon, Q., Fatemi, S., & Simon, S. (2020). Variability in the energetic electron bombardment of Ganymede. *Journal of Geophysical Research: Space Physics*, 125(9), 1–35. <https://doi.org/10.1029/2020JA028347>
- Liuzzo, L., Simon, S., Feyerabend, M., & Motschmann, U. (2017). Magnetic signatures of plasma interaction and induction at Callisto: The Galileo C21, C22, C23, and C30 flybys. *Journal of Geophysical Research: Space Physics*, 122(7), 7364–7386. <https://doi.org/10.1002/2017JA024303>
- Liuzzo, L., Simon, S., & Feyerabend, M. (2018). Observability of Callisto's inductive signature during the Jupiter ICy Moons explorer mission. *Journal of Geophysical Research: Space Physics*, 123(11), 9045–9054. <https://doi.org/10.1029/2018JA025951>
- Liuzzo, L., Simon, S., Feyerabend, M., & Motschmann, U. (2016). Disentangling plasma interaction and induction signatures at Callisto: The Galileo C10 flyby. *Journal of Geophysical Research: Space Physics*, 121(9), 8677–8694. <https://doi.org/10.1002/2016JA023236>

- Liuzzo, L., Simon, S., & Regoli, L. (2019a). Energetic electron dynamics near Callisto. *Planetary and Space Science*, *179*, 104726. <https://doi.org/10.1016/j.pss.2019.104726>
- Liuzzo, L., Simon, S., & Regoli, L. (2019b). Energetic ion dynamics near Callisto. *Planetary and Space Science*, *166*, 23–53. <https://doi.org/10.1016/j.pss.2018.07.014>
- Mauk, B. H., Haggerty, D. K., Jaskulek, S. E., Schlemm, C. E., Brown, L. E., Cooper, S. A., et al. (2017). The Jupiter Energetic Particle Detector Instrument (JEDI) investigation for the Juno mission. *Space Science Reviews*, *213*(1–4), 289–346. <https://doi.org/10.1007/s11214-013-0025-3>
- Mauk, B. H., Mitchell, D. G., McEntire, R. W., Paranicas, C. P., Roelof, E. C., Williams, D. J., & Lagg, A. (2004). Energetic ion characteristics and neutral gas interactions in Jupiter's magnetosphere. *Journal of Geophysical Research*, *109*(A9), A09S12. <https://doi.org/10.1029/2003JA010270>
- Menietti, J. D., Shprits, Y. Y., Horne, R. B., Woodfield, E. E., Hospodarsky, G. B., & Gurnett, D. A. (2012). Chorus, ECH, and Z mode emissions observed at Jupiter and Saturn and possible electron acceleration. *Journal of Geophysical Research*, *117*(A12). <https://doi.org/10.1029/2012JA018187>
- Modolo, R., & Chanteur, G. M. M. (2008). A global hybrid model for Titan's interaction with the Kronian plasma: Application to the Cassini T<sub>9</sub> flyby. *Journal of Geophysical Research*, *113*(A1). <https://doi.org/10.1029/2007JA012453>
- Müller, J., Simon, S., Motschmann, U., Schüle, J., Glassmeier, K. H., & Pringle, G. J. (2011). AIKEF: Adaptive hybrid model for space plasma simulations. *Computer Physics Communications*, *182*(4), 946–966. <https://doi.org/10.1016/j.cpc.2010.12.033>
- Nénon, Q., Miller, L. P., Kollmann, P., Liuzzo, L., Pinto, M., & Witasse, O. (2022). Pitch angle distribution of MeV electrons in the magnetosphere of Jupiter. *Journal of Geophysical Research: Space Physics*, *127*(8). <https://doi.org/10.1029/2022JA030627>
- Neubauer, F. (1980). Nonlinear standing Alfvén wave current system at Io: Theory. *Journal of Geophysical Research*, *85*(9), 1171–1178. <https://doi.org/10.1029/JA085iA03p01171>
- Neubauer, F. (1998). The sub-Alfvénic interaction of the Galilean satellites with the Jovian magnetosphere. *Journal of Geophysical Research*, *103*(E9), 843–866. <https://doi.org/10.1029/97JE03370>
- Paranicas, C., Hibbitts, C. A., Kollmann, P., Ligier, N., Hendrix, A. R., Nordheim, T. A., et al. (2018). Magnetospheric considerations for solar system ice state. *Icarus*, *302*, 560–564. <https://doi.org/10.1016/j.icarus.2017.12.013>
- Paranicas, C., Mauk, B. H., Kollmann, P., Clark, G., Haggerty, D. K., Westlake, J., et al. (2022). Energetic charged particle fluxes relevant to Ganymede's polar region. *Geophysical Research Letters*. <https://doi.org/10.1029/2022GL098077>
- Paranicas, C., Roussos, E., Decker, R. B., Johnson, R. E., Hendrix, A. R., Schenk, P., et al. (2014). The lens feature on the inner saturnian satellites. *Icarus*, *234*, 155–161. <https://doi.org/10.1016/j.icarus.2014.02.026>
- Paranicas, C., Szalay, J. R., Mauk, B. H., Clark, G., Kollmann, P., Haggerty, D. K., et al. (2021). Energy spectra near Ganymede from Juno data. *Geophysical Research Letters*, *48*(10), 1–7. <https://doi.org/10.1029/2021GL093021>
- Plainaki, C., Massetti, S., Jia, X., Mura, A., Milillo, A., Grassi, D., et al. (2020). Kinetic simulations of the Jovian energetic ion circulation around Ganymede. *The Astrophysical Journal*, *900*(1), 74. <https://doi.org/10.3847/1538-4357/aba94c>
- Plainaki, C., Milillo, A., Massetti, S., Mura, A., Jia, X., Orsini, S., et al. (2015). The H<sub>2</sub>O and O<sub>2</sub> exospheres of Ganymede: The result of a complex interaction between the jovian magnetospheric ions and the icy moon. *Icarus*, *245*, 306–319. <https://doi.org/10.1016/j.icarus.2014.09.018>
- Poppe, A. R., Fatemi, S., & Khurana, K. K. (2018). Thermal and energetic ion dynamics in Ganymede's magnetosphere. *Journal of Geophysical Research: Space Physics*, *123*(6), 4614–4637. <https://doi.org/10.1029/2018JA025312>
- Regoli, L. H., Roussos, E., Feyerabend, M., Jones, G. H., Krupp, N., Coates, A. J., et al. (2016). Access of energetic particles to Titan's exobase: A study of Cassini's T<sub>9</sub> flyby. *Planetary and Space Science*, *130*, 40–53. <https://doi.org/10.1016/j.pss.2015.11.013>
- Richards, P. C. G., Fennelly, J. A. a., & Torr, D. G. G. (1994). EUVAC: A solar EUV flux model for aeronomic calculations. *Journal of Geophysical Research*, *99*(A5), 8981–8992. <https://doi.org/10.1029/94JA00518>
- Roederer, J. G. (1967). On the adiabatic motion of energetic particles in a model magnetosphere. *Journal of Geophysical Research*, *72*(3), 981–992. <https://doi.org/10.1029/jz072i003p00981>
- Roth, L., Alday, J., Becker, T. M., Ivchenko, N., & Retherford, K. D. (2017). Detection of a hydrogen corona at Callisto. *Journal of Geophysical Research: Planets*, *122*(5), 1046–1055. <https://doi.org/10.1002/2017JE005294>
- Saur, J., Janser, S., Schreiner, A., Clark, G., Mauk, B. H., Kollmann, P., et al. (2018). Wave-particle interaction of Alfvén waves in Jupiter's magnetosphere: Auroral and magnetospheric particle acceleration. *Journal of Geophysical Research: Space Physics*, *123*(11), 9560–9573. <https://doi.org/10.1029/2018JA025948>
- Seufert, M., Saur, J., & Neubauer, F. M. (2011). Multi-frequency electromagnetic sounding of the Galilean moons. *Icarus*, *214*(2), 477–494. <https://doi.org/10.1016/j.icarus.2011.03.017>
- Shprits, Y. Y., Menietti, J. D., Drozdov, A. Y., Horne, R. B., Woodfield, E. E., Groene, J. B., et al. (2018). Strong whistler mode waves observed in the vicinity of Jupiter's moons. *Nature Communications*, *9*(1), 7–12. <https://doi.org/10.1038/s41467-018-05431-x>
- Simon, S., Addison, P., & Liuzzo, L. (2022). Formation of a displaced plasma wake at Neptune's Moon Triton. *Journal of Geophysical Research: Space Physics*, *127*(1). <https://doi.org/10.1029/2021JA029958>
- Snowden, D., & Higgins, A. (2021). A Monte Carlo model of energy deposition, ionization, and sputtering due to thermal ion precipitation into Titan's upper atmosphere. *Icarus*, *354*, 113929. <https://doi.org/10.1016/j.icarus.2020.113929>
- Snowden, D., Smith, M., Jimson, T., & Higgins, A. (2018). Energy deposition and ion production from thermal oxygen ion precipitation during Cassini's T57 flyby. *Icarus*, *305*, 186–197. <https://doi.org/10.1016/j.icarus.2018.01.014>
- Snowden, D., & Yelle, R. V. (2014). The thermal structure of Titan's upper atmosphere, II: Energetics. *Icarus*, *228*, 64–77. <https://doi.org/10.1016/j.icarus.2013.08.027>
- Strobel, D. F., Saur, J., Feldman, P. D., & McGrath, M. A. (2002). Hubble space Telescope space Telescope imaging Spectrograph search for an atmosphere on Callisto: A Jovian unipolar inductor. *The Astrophysical Journal*, *581*(1), 51–54. <https://doi.org/10.1086/345803>
- Styczinski, M. J., Vance, S. D., Harnett, E. M., & Cochrane, C. J. (2022). A perturbation method for evaluating the magnetic field induced from an arbitrary, asymmetric ocean world analytically. *Icarus*, *376*, 114840. <https://doi.org/10.1016/j.icarus.2021.114840>
- Takeuchi, S. (2002). Relativistic E × B acceleration. *Physical Review E—Statistical, Nonlinear and Soft Matter Physics*, *66*(3), 2–5. <https://doi.org/10.1103/PhysRevE.66.037402>
- Vance, S. D., Styczinski, M. J., Bills, B. G., Cochrane, C. J., Soderlund, K. M., Gómez-Pérez, N., & Paty, C. (2021). Magnetic induction responses of Jupiter's Ocean Moons including effects from adiabatic convection. *Journal of Geophysical Research: Planets*, *126*(2), 1–25. <https://doi.org/10.1029/2020JE006418>
- Vay, J.-L. (2008). Simulation of beams or plasmas crossing at relativistic velocity. *Physics of Plasmas*, *15*(5), 056701. <https://doi.org/10.1063/1.2837054>
- Vorburger, A., Fatemi, S., Galli, A., Liuzzo, L., Poppe, A. R., & Wurz, P. (2022). 3D Monte-Carlo simulation of Ganymede's water exosphere. *Icarus*, *375*, 114810. <https://doi.org/10.1016/j.icarus.2021.114810>

- Vorburger, A., Pflieger, M., Lindkvist, J., Holmström, M., Lammer, H., Lichtenegger, H. I., et al. (2019). 3D-modeling of Callisto's surface sputtered exosphere environment. *Journal of Geophysical Research: Space Physics*, *124*(8), 7157–7169. <https://doi.org/10.1029/2019JA026610>
- Williams, D. J., Mauk, B., & McEntire, R. W. (1997). Trapped electrons in Ganymede's magnetic field. *Geophysical Research Letters*, *24*(23), 2953–2956. <https://doi.org/10.1029/97GL03003>
- Wulms, V., Saur, J., Strobel, D. F., Simon, S., & Mitchell, D. G. (2010). Energetic neutral atoms from Titan: Particle simulations in draped magnetic and electric fields. *Journal of Geophysical Research*, *115*(A6), 1–18. <https://doi.org/10.1029/2009JA014893>
- Xiao, F., Shen, C., Wang, Y., Zheng, H., & Wang, S. (2008). Energetic electron distributions fitted with a relativistic kappa-type function at geosynchronous orbit. *Journal of Geophysical Research*, *113*(5), 1–10. <https://doi.org/10.1029/2007JA012903>
- Zimmer, C., Khurana, K. K., & Kivelson, M. G. (2000). Subsurface Oceans on Europa and Callisto: Constraints from Galileo magnetometer observations. *Icarus*, *347*(2), 329–347. <https://doi.org/10.1006/icar.2000.6456>